1-1-2005

Entrainment in the trailing edge cavity of high-lift wings

Johanna Christine Malisani
Ryerson University

ENTRAINMENT IN THE TRAILING EDGE CAVITY OF HIGH-LIFT WINGS

By

Johanna Christine Malisani,
Bachelor of Engineering, Ryerson, 2003

A report

presented to Ryerson University

in partial fulfillment of the

requirements for the degree of

Master of Engineering

in the Program of

Mechanical Engineering

Toronto, Ontario, Canada, 2005

AUTHOR'S DECLARATION

I hereby declare that I am the sole author of this thesis.

I authorize Ryerson University to lend this thesis to other institutions or individuals for the purpose of scholarly research.

I further authorize Ryerson University to reproduce this thesis by photocopying or by other means, in total or in part, at the request of other institutions or individuals for the purpose of scholarly research.

Entrainment in the Trailing Edge Cavity of High-Lift Wings
Johanna C. Malisani, Masters of Engineering, 2005
Mechanical Engineering, Ryerson University

ABSTRACT

The essence of this project is a computational fluid dynamics analysis of the trailing edge cavity of high-lift wings. The objective is to investigate the effects on the resulting flow field in the trailing edge cavity as the bute's length and deflection angle are altered. Of notable interest was the effect this had on the overall performance of the wing, as indicated by the lift coefficient. Also of keen interest was the effect of flow entrainment in the trailing edge cavity on the lift coefficient. In addition to the base case, the current trailing edge device configuration, four other cases were considered for angles of attack of –5, 0, 5, and 10 degrees. The first case analyzed was that for a bute of half-length, the second case, a bute of three-quarters length, the third case, a bute with a 25.45 degree deflection angle and the fourth case, a bute with a 45.45 degree deflection angle. All the cases were examined at a Mach number of 0.28 and compared to the base case. It was found that the 25.45 degree deflected bute case had the best lift qualities for all angles of attack. This is attributed to the fact that the high-energy flow from the bottom surface of the wing remains attached to the bute over a greater portion of it's length, thus delaying the boundary layer separation on the bute. By delaying the separation, the flow is better directed toward the slot passages of the trailing edge device, so that upper surface flow can be re-energized, stabilizing the boundary layer, and suppressing the onset of separation. It was also discovered that entrainment can be beneficial if the recirculation zones are appropriately located in the cavity, as these recirculation zones can further accelerate the high-speed flow from the bottom surface through the slot passages, to allow for greater control of the boundary layer.

ACKNOWLEDGEMENTS

The author would like to thank Dr. Paul Walsh for his guidance, knowledge, and support throughout the duration of this project.

The author would to thank Mr. Peter Hodal for his help and guidance during the initial stages of this project.

DEDICATIONS

This work is dedicated to all those who have guided, helped, and supported me. These include, in particular, my undergraduate thesis advisor and masters project supervisor, Paul Walsh, my coach, Valerie Barker, my sister, Laura, and my parents, Norman and Debbie who always encouraged me in my quest to achieve my dreams.

TABLE OF CONTENTS

Page

LIST OF TABLES

LIST OF FIGURES

NOMENCLATURE, ABBREVIATIONS, ACRONYMS

C_D	drag coefficient
CFD	computational fluid dynamics
C_L	lift coefficient
C_{Lmax}	maximum lift coefficient
C_p	specific heat at constant pressure
M	Mach number
R_e	Reynolds number
S	wing surface area
V_{stall}	stall speed
W	aircraft weight

GREEK NOMENCLATURE

α	angle of attack
ρ	density
δ_f	flap deflection angle

CHAPTER 1: INTRODUCTION

1.1 Introduction

Everyday, millions of air travelers around the world, prior to takeoff and on approach for landing, hear the noise associated with the hydraulic systems deploying the high-lift systems of the aircraft. The average air traveler knows that flaps and slats, the two components of high-lift systems used on today's aircraft, whether they are large commercial airliners or small private planes, are used during takeoff and landing. However, they do not understand why these high-lift systems are needed and why they are specifically used during takeoff and landing.

1.1.1 Why High-Lift?

High-lift systems are employed during takeoff and landing, when the aircraft speed is low, when producing and maintaining sufficient lift to keep the aircraft airborne is critical. The important parameter in producing and maintaining lift is the stall speed, and it is defined as follows:

$$V_{stall} = \sqrt{\frac{2W}{\rho S C_{L_{max}}}} \quad (1)$$

where W is the weight of the aircraft, ρ is the density of the air, S is the wing planform area, and C_{Lmax} is the maximum lift coefficient which is a function of the maximum angle of attack that can be achieved prior to the onset of stall conditions. The stall speed determines the field length required for takeoff and landing. To minimize the field length, the stall speed must also be minimized. There are several ways to minimize the stall speed based on equation (1); reduce the weight of the aircraft, increase the surface area of the wing, and or increase the maximum lift coefficient, C_{Lmax}. Decreasing the weight is a difficult task, as it is a function of the physical structure of the aircraft (which is already minimized), the cargo, and fuel on board. Increasing the surface area of the wing incurs a weight penalty, as well as increases drag, thus hindering cruise performance. The most practical option is then to increase the maximum lift coefficient.

High-lift systems are designed to do just this: increase the maximum lift coefficient needed for takeoff and landing, while maintaining good cruise efficiency. High-lift devices, as described by Abbot and Von Doenhoff [1], are essentially movable elements that permit the pilot to change the geometry and aerodynamic characteristics of the wing sections to control the motion of the airplane or to improve the performance in some desired manner. The desire to improve the performance by increasing the wing loading while maintaining acceptable landing and take-off speeds led to the development of retractable devices to improve the maximum lift coefficients of wings without changing the characteristics for the cruising and high-speed flight conditions [1]. There are several types of retractable devices that have been developed over the years, trailing edge devices and leading edge devices, which increase the wing loading and C_{Lmax}. In the retracted position, the high-lift system minimally adds to the drag and therefore good cruise performance is maintained. For takeoff and landing, the system can be extended in numerous configurations to achieve the highest possible lift, with the associated drag penalty. For landing, the additional drag is welcomed, as it enables the pilot to increase the approach angle to safely pass over high obstacles and barriers.

1.2 Review of Trailing Edge Configurations

1.2.1 High-Lift Aerodynamics

High-lift aerodynamics is very complex, involving the behaviour of the boundary layer, compressibility effects, and the aerodynamic effects of additional elements of the high-lift system employed. In considering the aerodynamics and flow phenomena of trailing edge high-lift devices; separation, recirculation and the mixing of the viscous layers of the various elements of the trailing edge device needed to be considered and accurately modeled

In general, there are two ways in which trailing edge devices can increase the maximum lift coefficient C_{Lmax}. One, they increase camber and two, they increase the surface area. The increase in camber changes the pressure distribution over the surface of the airfoil, while the increase in surface area allows more lift to be carried over the aft portion of the airfoil.

As noted above, there are several types of trailing edge devices and they are illustrated below in Figures 1 and 2. From Figure 1, the plain and split flap systems, when deflected downward, increase the camber of the airfoil, thereby increasing C_{Lmax}. The more the flap is deflected, the greater the increase in camber and the greater the C_{Lmax}. However, it should be noted that the maximum lift occurs at a smaller angle of attack than the plain cruise configuration airfoil and is illustrated below in Figure 3. From Figure 1, the slotted and Fowler flap systems, and from Figure 2, the double slotted and Calderon flap systems deflect downward, they also extend beyond the original chord length of the plain cruise configuration airfoil when deployed. The extension of the flap beyond the original chord length increases the wing area, in addition to increasing the camber, thereby further increasing C_{Lmax}. Again, for the slotted Fowler

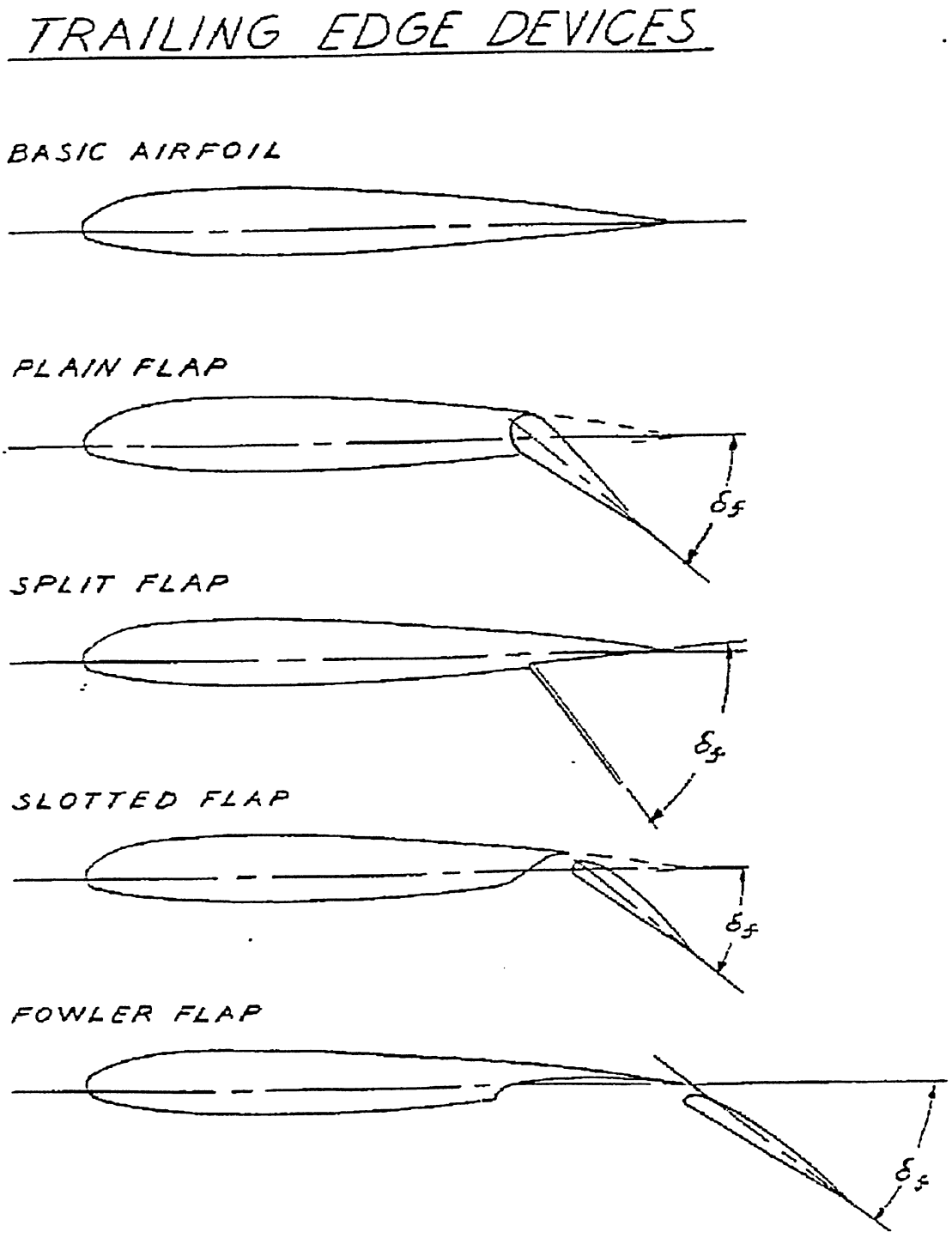

Figure 1: Basic Trailing Edge Devices [2]

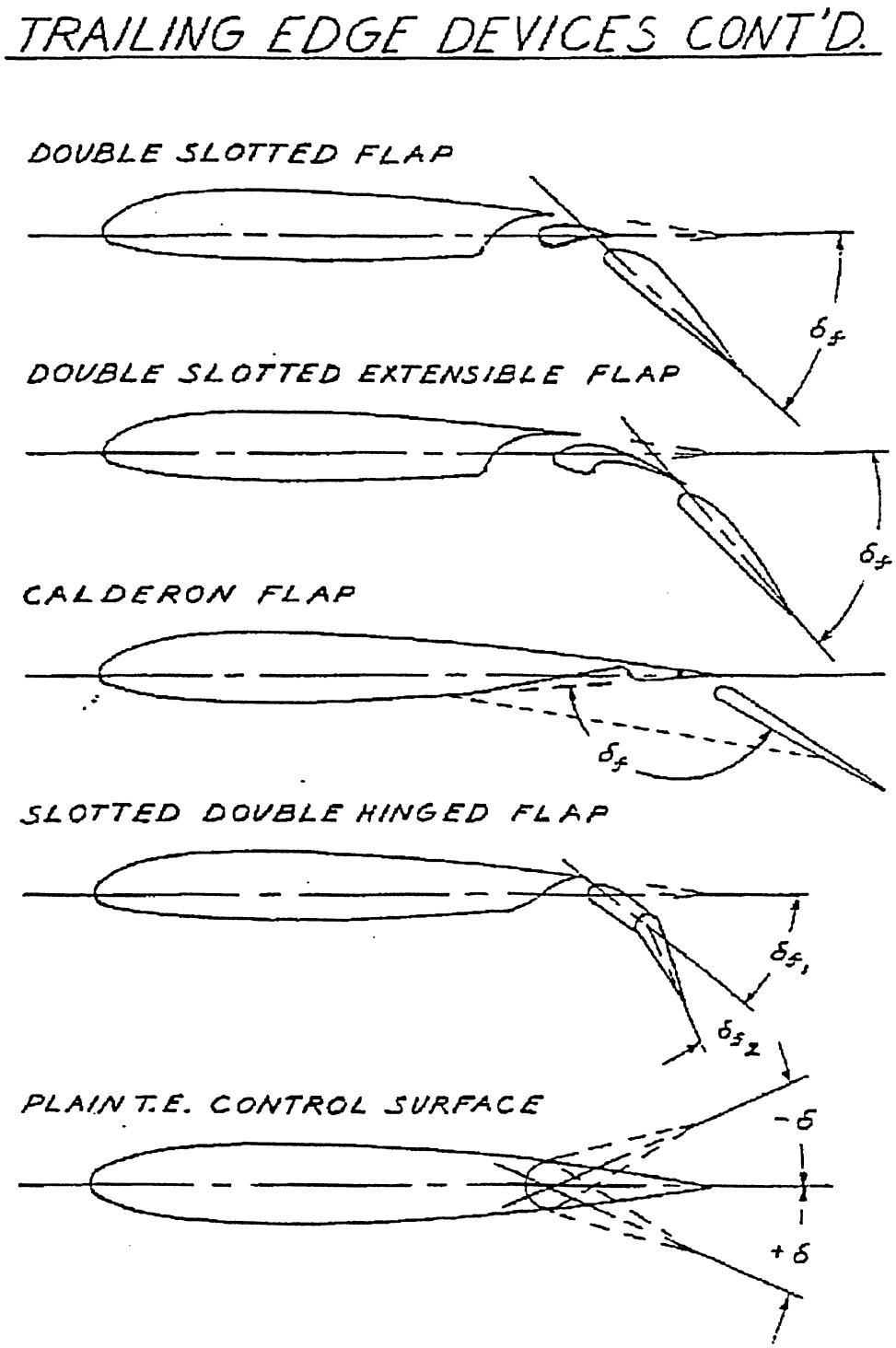

Figure 2: Trailing Edge Devices [2]

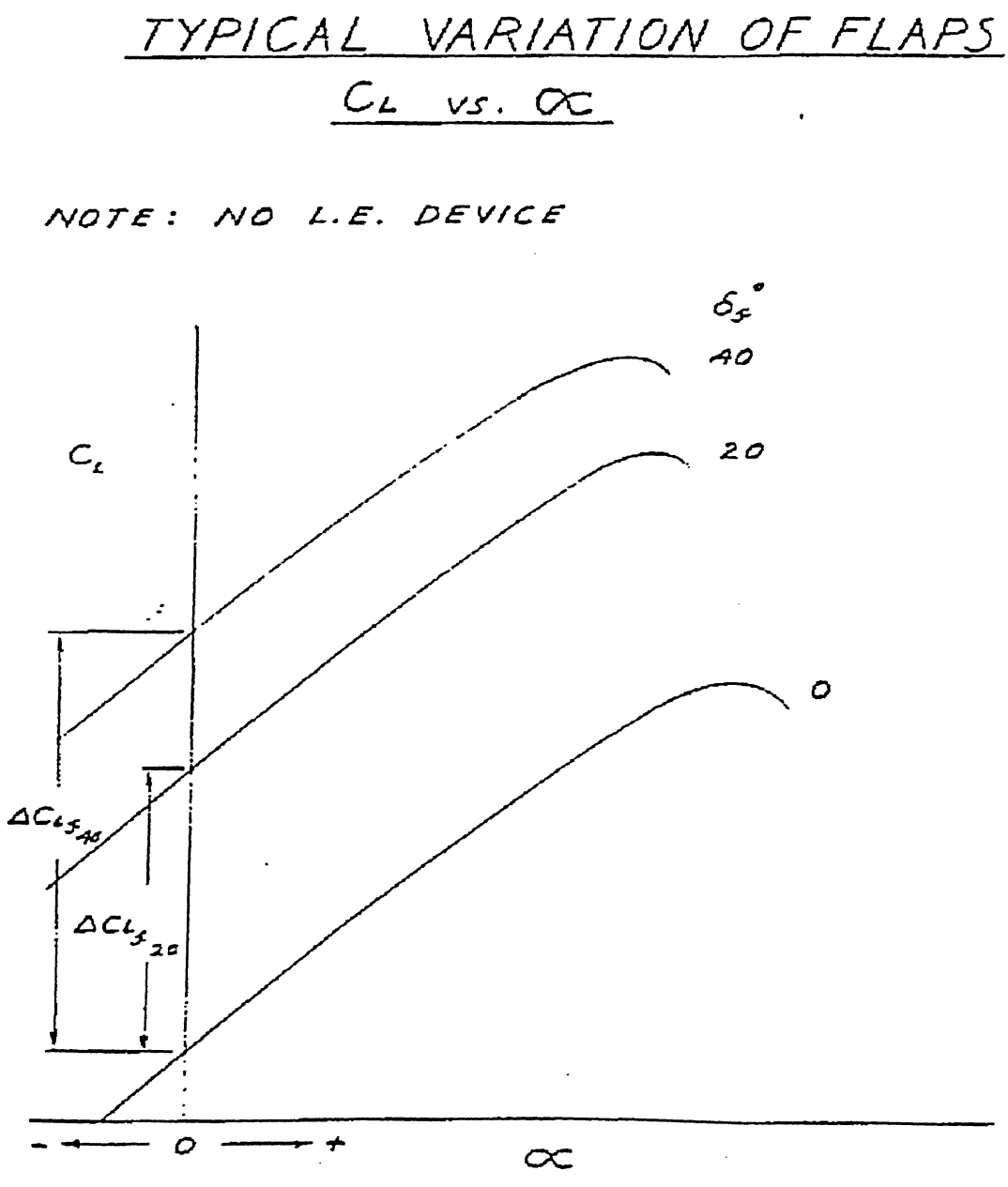

Figure 3: Typical Effect of Flaps on the Lift Curve Slope [2]

motion flap systems, the maximum lift occurs at a smaller angle of attack than the plain cruise configuration airfoil as illustrated below in Figure 4. Therefore, from Figures 3 and 4, it can be seen that flaps can increase the camber and surface area and also effectively increase the angle of attack.

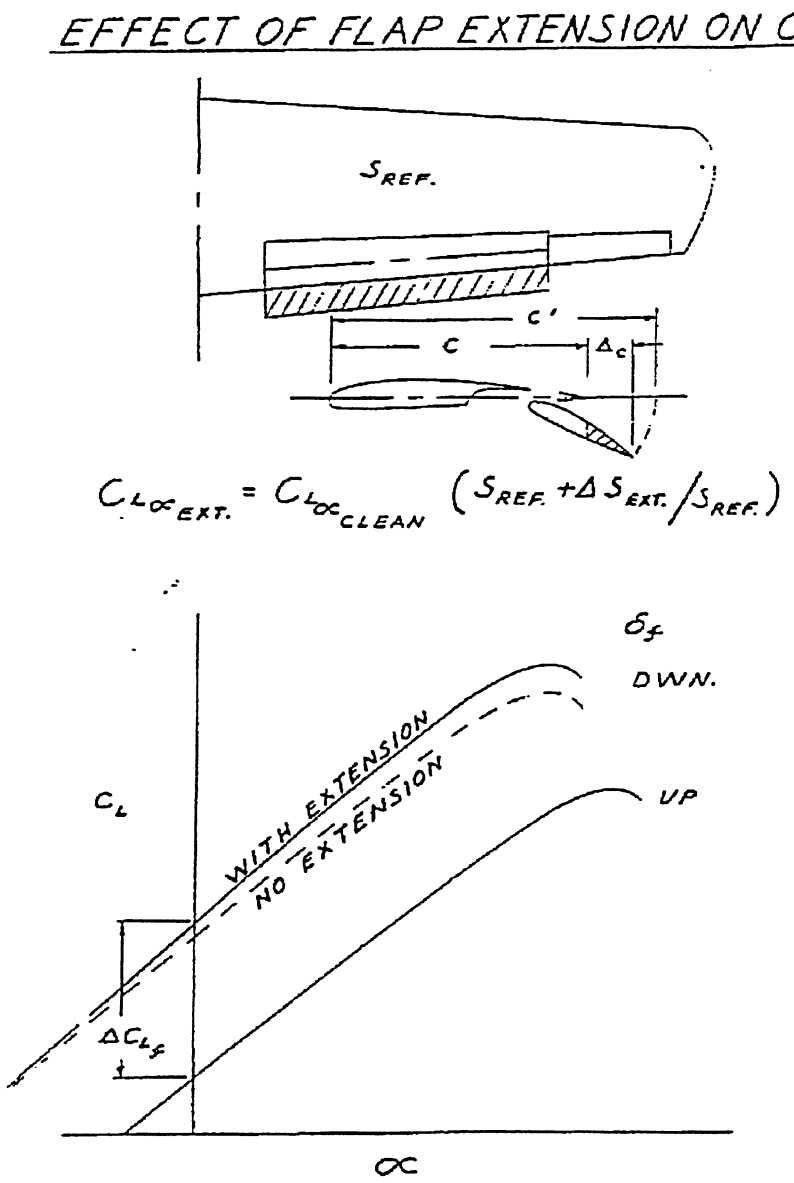

Figure 4: The Effect of Flap Extension on the Lift Curve Slope [2]

1.2.2 Blunt Trailing Edges

The creation of a blunt trailing edge on an airfoil is a non-mechanical means of improving aerodynamic performance. According to Lotz et al. [3], DTE (divergent trailing edge – a type of blunt trailing edge) airfoils are designed by increasing the airfoil thickness over the aft 10% of chord such that suction- and pressure-side flows are diverging from each other at the trailing edge. This modification to a blunt supercritical

airfoil effects an increase in the effective chord by lengthening the recirculation in the wake with the result that the lift-to-drag ratio is increased, which significantly benefits airfoil and wing aerodynamic performance. Thompson and Lotz [4] also state that DTE airfoils have a larger pressure difference between the suction and pressure sides in the trailing edge region than conventional supercritical airfoils. They indicate in reference [4] that this pressure jump causes a reduction in the angle of attack at the design lift coefficient for speeds near the drag-rise Mach number that leads to an increase in aerodynamic efficiency in transonic cruise.

1.2.3 Split Flaps

Split flaps are one of the simplest of the high-lift devices. A split flap is simply deflecting the aft portion of the lower airfoil surface at a hinge point on the forward surface of the deflected portion or flap. The split flap is typically twenty percent of the chord length and is hinged at eighty percent of the chord length. The split flap as mentioned above, increases the camber and C_{Lmax}; however, it also greatly increases the drag, as it creates a bluff body.

1.2.4 Gurney Flaps

Gurney flaps are also simple high-lift devices. A Gurney flap is a short plate attached to the trailing edge perpendicular to the chordline on the pressure side (lower surface) of the airfoil as shown below in Figure 5. The Gurney flap increases lift by turning the flow downward to relieve the adverse pressure gradient near the trailing edge, thus increasing the suction over the upper surface [5]. In the study by Li et al. [5], it was found that the Gurney flap substantially increased the maximum lift coefficient of the cropped nonslender delta wing and attributed this to the fact that the Gurney flap served to increase the effective camber of the wing. It was also found that the stall angle decreased, while the zero-lift angle of attack became increasingly more negative. Li et al [5] concluded that, at low-to-moderate lift coefficients, the Gurney flap produced more drag than the clean wing, whereas, at high lift coefficients, the Gurney flap was able to achieve very high lift with less drag than the clean wing. In Li et al.'s [6] study on the

effects of Gurney Flaps on a NACA0012 Airfoil, they investigated the effect various Gurney flap heights (based on the percent chord length of the NACA0012 airfoil). They found that Gurney flaps significantly increased the maximum lift coefficient, that the stall angle decreased, and that the Gurney flap increased the effective camber of the airfoil. They also determined that the Gurney flap provided an increase in the lift-to-drag ratio in comparison to the clean (plain cruise configuration) airfoil. They concluded the Gurney flap increased the upper surface suction and the lower surface high pressure, causing the enhancement in lift. Finally, they found that the addition of the Gurney flap resulted in the downward turning of the flow aft of the airfoil, which thereby increased the effective camber of the airfoil.

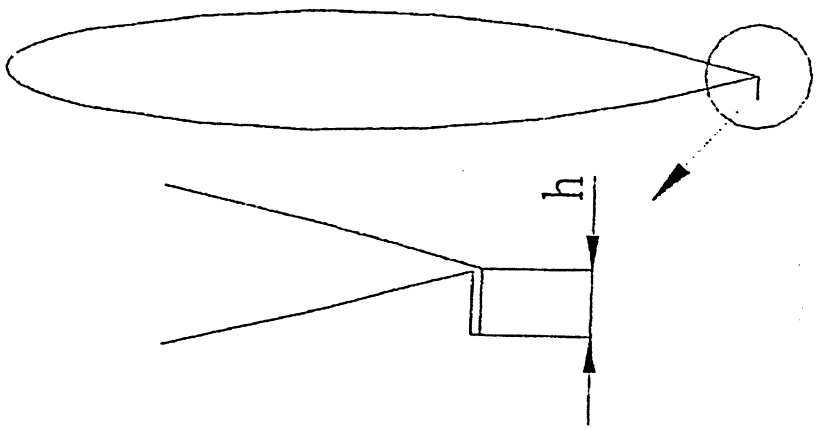

Figure 5: Gurney Flap Configuration [5]

1.2.5 Slotted Flaps

Slotted flaps create one or more slots between the main airfoil section and the deflected flap system. These slots duct the air from the bottom surface to the upper surface of the wing in such a way as to delay the separation of the airflow over the flap by re-energizing the boundary layer, thereby controlling the onset of stall.

As noted previously and as illustrated in Figure 2, there are several types of slotted flaps, and they are primarily classified according to the number of slots. The single-slotted flap is the simplest and is widely used on general aviation aircraft. Double and triple-slotted flaps are typically used on commercial aircraft. In the design of slotted flaps, it is important to consider how far aft the flap moves as it is deflected. The flap

movement can vary from simple rotation about a fixed point to the combination of rotation and translation such that the leading edge of the flap moves to the normal trailing edge position. This translated aft motion of the flap requires that the upper surface be extended over the flap in the stowed or retracted position. This extension of the upper surface is called the "lip", which is depicted in Figure 6, and it directs high-speed airflow from the lower surface of the airfoil through the slot to the upper surface to renew the lost kinetic energy.

In the design of single-slotted flaps, the two design parameters need to be considered. One is the chord-wise position of the lip, and the other is the shape of the slot passage. The maximum lift coefficient, C_{Lmax}, increases as the lip position approaches the trailing edge of the wing section. The shape of the slot passage effects how well the boundary layer is re-energized by the airflow, thereby affecting C_{Lmax}. The more efficiently airflow passes through the slot passage, the better the regeneration of the boundary layer and therefore the greater the increase in C_{Lmax}.

Double-slotted flaps have two slot passages. The additional slot passage is created by the addition of a fore flap or vane. The double-slotted flap produces a significant increase in the maximum lift coefficient over that obtainable by single-slotted flaps due to the fact that the vane of the double-slotted flap assists in turning the air downward over the main flap, thus delaying the stall of the flap to higher deflections [1]. The higher C_{Lmax} is achieved and attributed to the vane, as it provides greater stability to the boundary layer as it is re-energized twice by the high-speed flow from the lower surface. Hodal notes that the design of the slot shape is critical as the aerodynamics that govern the flow by the slotted flap are extremely sensitive to changes in slot geometry and configuration [7].

Extensive experimental work, via wind tunnel testing, was undertaken in the late 1930's and early 1940's by the National Advisory Committee for Aeronautics (NACA) on various airfoil shapes and airfoils with various flap configurations. Much of this research is compiled and summarized by Ira Abbot and Albert Von Doenhoff in Theory of Wing Sections [1].

In Hodal's study [7] of the Boeing 717 high-lift devices, which are a double-slotted flap arrangement, it was noted that the interaction of the main wing airfoil and the flap boundary layer has an effect on the flap pressure distribution. Hodal indicated that the close proximity of the wing wake to the upper surface of the flap causes the damping of the flap pressure distribution. He reported that the large viscous region created by the wake of the main airfoil has a displacement effect on the flow field above the flap by suppressing the inviscid core flow, inhibiting the development of the flap boundary layer. He stated that the amount of suppression is related to the thickness of the viscous region, which is dependent on the Reynolds number and the angle of attack. Hodal concluded that the bute configuration, shown in Figure 6 below, is also important, as it affects the direction of the core flow. The bute is the hinged portion of the bottom surface of the airfoil. When the trailing edge device is stowed in the trailing edge cavity, the bute is undeflected, creating the plain cruise configuration airfoil. When the trailing edge device is deployed, the bute is deflected upward, creating an obtuse angle with respect to the bottom surface of the airfoil. In the deflected position, the bute directs the bottom surface flow through the slot passages created by the spoiler, vane and flap. He indicated that in the undeflected position, only a small portion of the air stream made it through the first slot (between the spoiler and vane) resulting in a slightly lower overall lift when compared to the deflected bute. Hodal also concludes that, with the bute in the deflected position, flow separation occurs quickly, thereby causing the airflow to deflect from the path suggested by the bute angle.

In this study, the trailing edge device of a vane-flap configuration will be considered, with the focus on the effects the trailing edge device has on the flow field, specifically in the trailing edge cavity region, and how it affects the re-energizing of the boundary layer on the upper surface of the wing to prevent stall, thereby increasing C_{Lmax}. The vane-flap configuration under consideration in this study, the Boeing 717 high-lift device, is depicted in Figure 6, illustrating the main components of the trailing edge device and the flow passages. To model the complex flow field of the vane-flap

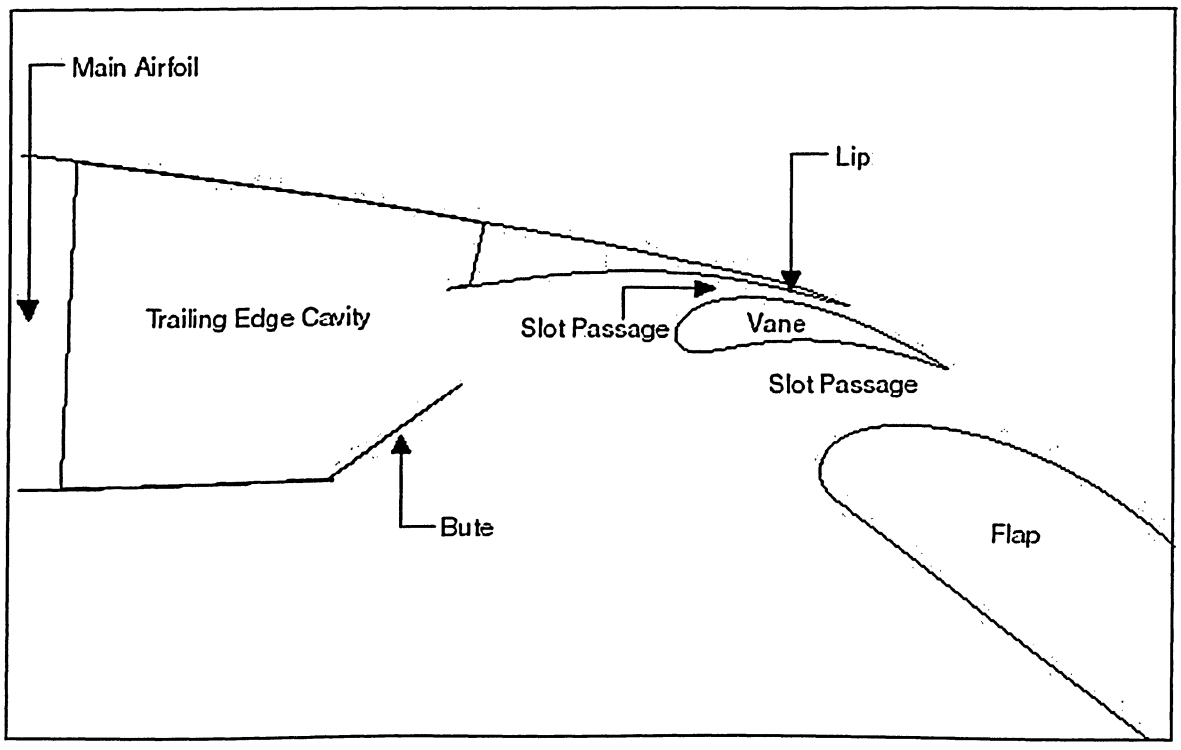

Figure 6: Boeing 717 High-Lift Device Configuration

configuration, computational fluid dynamics (CFD) software can be used to solve the governing equations and thus model the effects of separation, recirculation, and the mixing of the viscous layers.

1.3 Objectives

The complex flow field of the high-lift system of the Boeing 717 airfoil will be modeled via FLUENT, a CFD software package that can solve the full Navier-Stokes equations with turbulence effects. There are several objectives to this project and they are listed below:

1. CFD (FLUENT) software validation, via the simulation of the NACA 0012 airfoil for various Reynolds Numbers ($3*10^6$, $6*10^6$ and $9*10^6$) and the NACA0012 airfoil with a 60° deflected split flap ($R_e=6*10^6$) and comparison with published data.

2. Determination of the recirculation zones in the trailing edge cavity - how the angle of attack, the bute length and bute deflection angle affect these recirculation zones.
3. Determination of how much mass gets entrained in the trailing edge cavity - how the angle of attack, the bute length and bute deflection angle affects how much mass is entrained. It is assumed that the amount of mass entrainment is proportional to the amount of contaminants deposited in the trailing edge cavity.
4. Determination of the aerodynamic coefficients (C_L, C_D) – how the recirculation zones, flow entrainment, the angle of attack, the bute length and bute deflection angle affects these coefficients.

1.4 Synopsis

In the proceeding chapters, the process and methodology to meet the above stated objectives will be outlined. This methodology forms the structure of the project, as it follows the process of necessary to carry out a CFD analysis. By use of this methodology to validate the CFD software, it is ensured that the data obtained in the analysis of the high-lift system of the Boeing 717 airfoil is also valid.

In Chapter 2, the development of the computational grid will be discussed. This is the crux of any CFD analysis and, for this project, the grid generation software used was GAMBIT. The problems associated with multi-element airfoil grid generation will be discussed and how those problems were overcome.

In Chapter 3, the solution procedure for the CFD analysis will be discussed in terms of the type of model flow solver, turbulence model, boundary conditions, and other parameters used to model the complex flow field of the Boeing 717 high-lift system.

In Chapter 4, the validation of the FLUENT software package will be discussed. In Chapter 5, the results obtained for the Boeing 717 high-lift system will be analyzed and discussed.

Finally, in Chapter 6, conclusions based on the results of this project will be discussed and recommendations for further study will be proposed.

CHAPTER 2: GRID GENERATION

2.1 Introduction

Prior to any problem being analyzed by a CFD software package such as FLUENT, a computational grid or mesh must be generated. The generation of such a grid is paramount to the quality and accuracy of the CFD analysis of the flow field under consideration. In order to accurately predict the flow around an aerodynamic configuration, it is necessary to resolve gradients in flow properties and, to achieve this, grid points must be clustered or distributed in the appropriate regions. The grid point clustering can be achieved a priori, by user knowledge of the flow field. In order to guarantee grid quality, it is also essential to ensure that grid cell skewness, aspect ratio, and grid stretching are not too severe [8]. By clustering grid points or cells in regions of high gradients, the flow is not only resolved appropriately, but ensures that the grid is economical and efficient (in terms of computational time and memory) in producing a converged solution.

Multi-element airfoils, such as the Boeing 717 high-lift system airfoil under evaluation in this project, pose a particular challenge to the grid generation process. An unstructured grid approach can easily deal with complex shapes, but it will yield higher

truncation errors if care is not taken to obtain a smooth mesh. The structured grid approach has the potential to lower the truncation errors. The unstructured grid approach has more overhead, in terms of the associated increases in memory required and computational time, making the technique too inefficient for this analysis. There is also a slight loss of accuracy associated with unstructured meshing, due to grid irregularity [7].

The structured grid approach, as illustrated in Figure 7 below, lends itself to accurate resolution of high gradient regions of the flow field. From Figure 7, it can be seen that the grid spacing normal (adjacent) to the wall is very fine, and, as the grid moves away from the wall (airfoil), the grid spacing gradually increases. This non-uniform structured grid approach accurately resolves the viscous effects of the boundary layer region without additional computation time, as it concentrates the computational domain in this area of importance to the CFD analysis. In Figure 7, the grid spacing along the wall is not as fine and such a fine resolution is not necessary along the chord-wise direction of the airfoil, as the gradients in this direction are not as high as those normal to the airfoil.

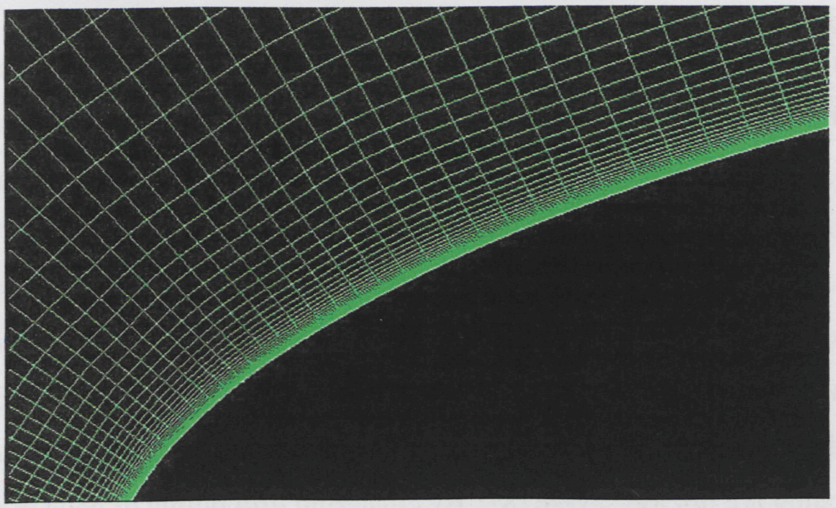

Figure 7: Structured Non-Uniform Grid with Fine Off-Wall Grid Spacing

Implementing a structured grid approach to a plain airfoil is a relatively trivial task; however, with multi-element airfoils, implementing the structured approach proves difficult because, as the geometry becomes more complex, the quality of the grid (as measured by skewness, stretching, cell aspect ratio etc.) decreases. Subsequently, in

general, deterioration in the performance and accuracy of the flow algorithm is experienced [8]. The following sections outline the methods used, in GAMBIT, to generate the grids for the various cases to be analyzed in this project.

2.2 Plain Airfoil

As mentioned in Chapter 1, part of the requirement for this project is the validation of the FLUENT CFD software package, and as such, the NACA0012 plain airfoil and the NACA0012 Split Flap airfoil were chosen. The structured grid approach was implemented to generate the computational domain or mesh. First, the NACA0012 plain airfoil will be looked at in detail and then the NACA0012 Split Flap will be considered.

2.3.1 NACA0012 Plain Airfoil

As mentioned in the previous section, implementing a structured grid to a plain airfoil is trivial; however, it is important to remember that grid quality is of the utmost importance and as such must follow the contours of the surface of the airfoil to appropriately resolve the viscous boundary layer. In that vein, it was necessary to ensure that the grid cells had little skewness and stretching, especially along the leading edge of the airfoil where there is significant curvature. The computational grid used to analyze the NACA0012 plain airfoil case is illustrated below in Figure 8.

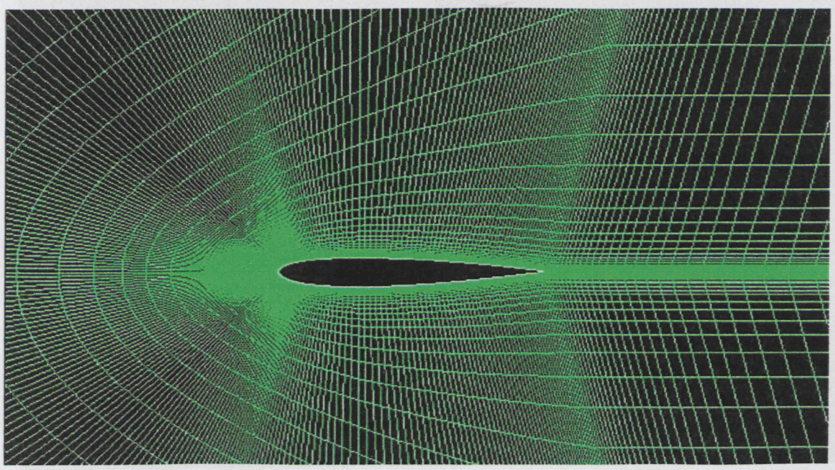

Figure 8: Grid for the NACA0012 Plain Airfoil Case

2.3.2 NACA0012 Split Flap Airfoil

The crux of this project is the analysis of high-lift devices, specifically flaps systems; it was necessary to validate results obtained from a previously studied flap system. As such, the NACA0012 Split Flap airfoil with a 60-degree deflection was chosen, as significant wind tunnel testing was carried out in the early 1940's and data were therefore readily available for comparison. Figure 9 illustrates the computational grid or mesh used to analyze the NACA0012 Split Flap airfoil. In order to maintain the quality of the grid around the flap to adequately resolve the boundary layer in this region, the grid had to follow the contour of the flap, and is illustrated below in Figure 10.

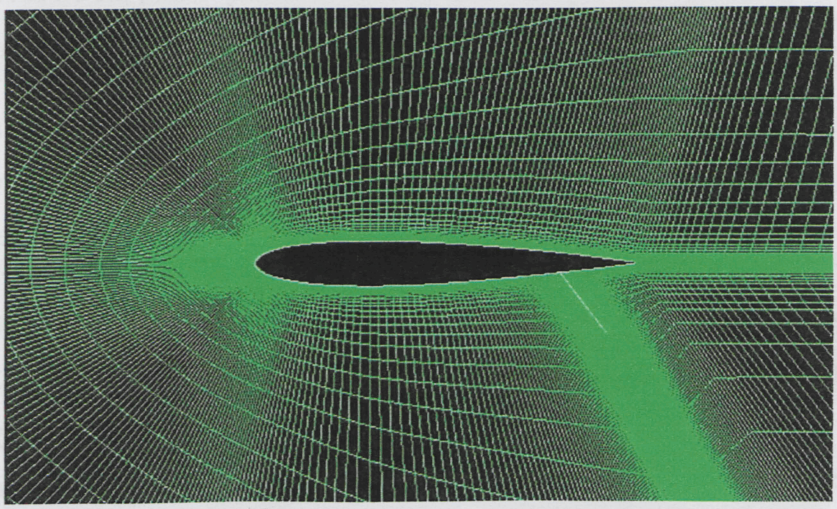

Figure 9: Grid for the NACA0012 Split Flap Airfoil Case

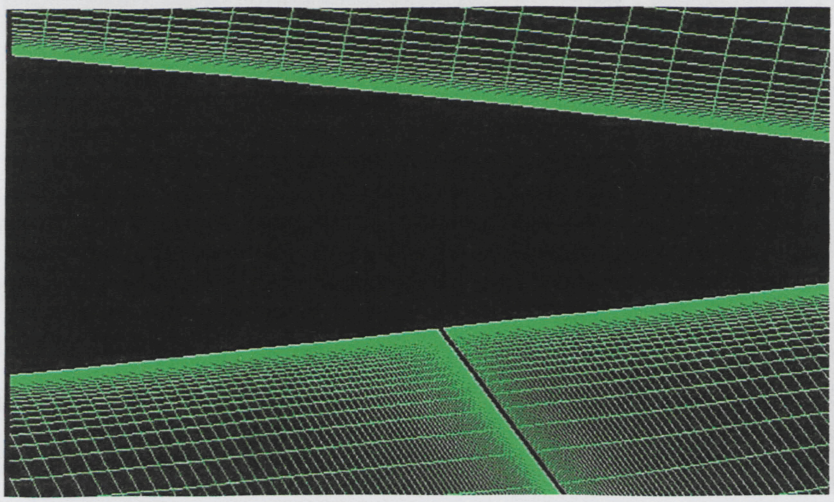

Figure 10: Grid around the Split Flap of the NACA0012 Split Flap Airfoil Case

2.3 Multi-Element Airfoils

As stated earlier in this chapter, multi-element airfoils pose a significant issue to grid quality in a structured mesh approach, as the interaction between grids of the various elements can cause cell skewness, stretching and high-aspect ratio cells leading to the degradation of the accuracy of the numerical solution. In order to overcome this issue, several techniques have been developed, namely, the multiblock grid and the embedded grid methods.

The multiblock method divides the computational domain into multiple blocks. From a grid quality perspective, it proves advantageous to define a topology around the airfoils, and in order to do that in a multiple element airfoil system, it is convenient to use C-type grid mesh zones around each element as shown below in Figure 11. In the multiblock technique, it is important that grid smoothness be maintained across the internal block boundaries as continuity across these boundaries is determined by the block-to-block information and data supplied on each side of every block to adjacent blocks and faces.

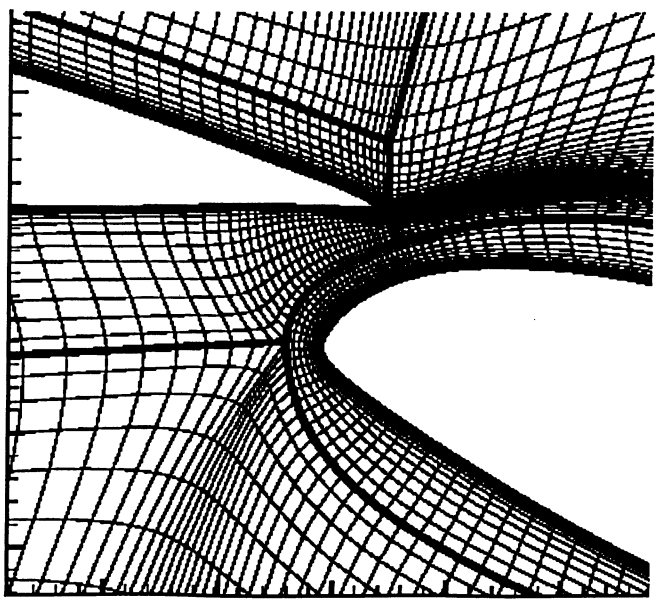

Figure 11: Example of C-Type Grid Zone around a Flap [9]

The grid embedding technique, also known as the chimera approach, involves the overlap of multiple blocks. The technique involves the addition or deletion of points in particular regions but is only feasible for complex three-dimensional geometries. The

implication of this technique is that the flow algorithm must be constructed so that it is capable of handling the interface of coarse to fine cells [8]. The data structure caused by the interface of coarse to fine cells is complicated and thus increases computation time and memory requirements to run the analysis. Since the embedded grid method has an inherent increase in computational time and memory, the multiblock method will be employed in this project to generate the computational grids.

2.3.1 Boeing 717 High-Lift System Airfoil

In implementing the multiblock zone technique to generate the mesh, it was first necessary to carefully create zones (faces in GAMBIT), in the vane-flap region, as shown below in Figure 12. These zones were then individually meshed so that the flow field could be appropriately resolved with minimal loss of grid quality.

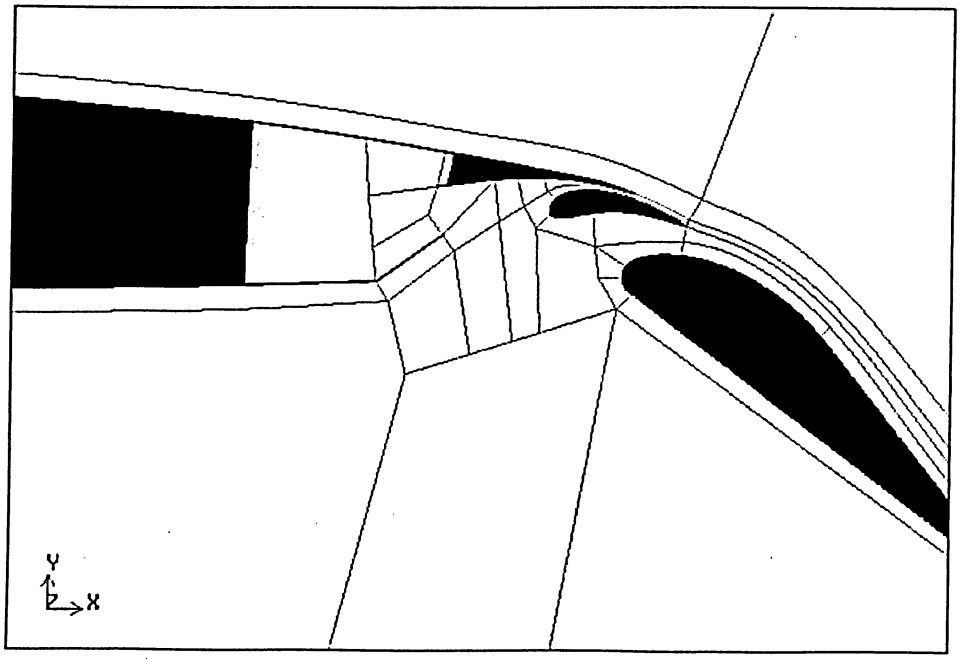

Figure 12: Breakdown of Computational Grid into Zones for the Boeing 717 High-Lift System in the Vane-Flap Region

The computational domain in essence emulates a wind tunnel, and as such, it is necessary to create a far-field boundary to model the steady freestream properties of the flow. The far-field boundary for all the cases analyzed was created using a parabolic shape, as there is no discontinuity in the slope. The apex of the parabola was situated 20

chord-lengths upstream of the leading edge of the airfoil and extended 30 chord-lengths aft of the leading edge. This ensured that the computational grid was sufficiently large enough to ensure that the steady freestream flow properties were attained to allow for the setting of the far-field boundary conditions. Figure 13 below, shows the computational grid domain used for all cases of the Boeing 717 high-lift system analyzed. The only significant differenece in the grids for the various cases is the zone break down in the vane-flap configuration.

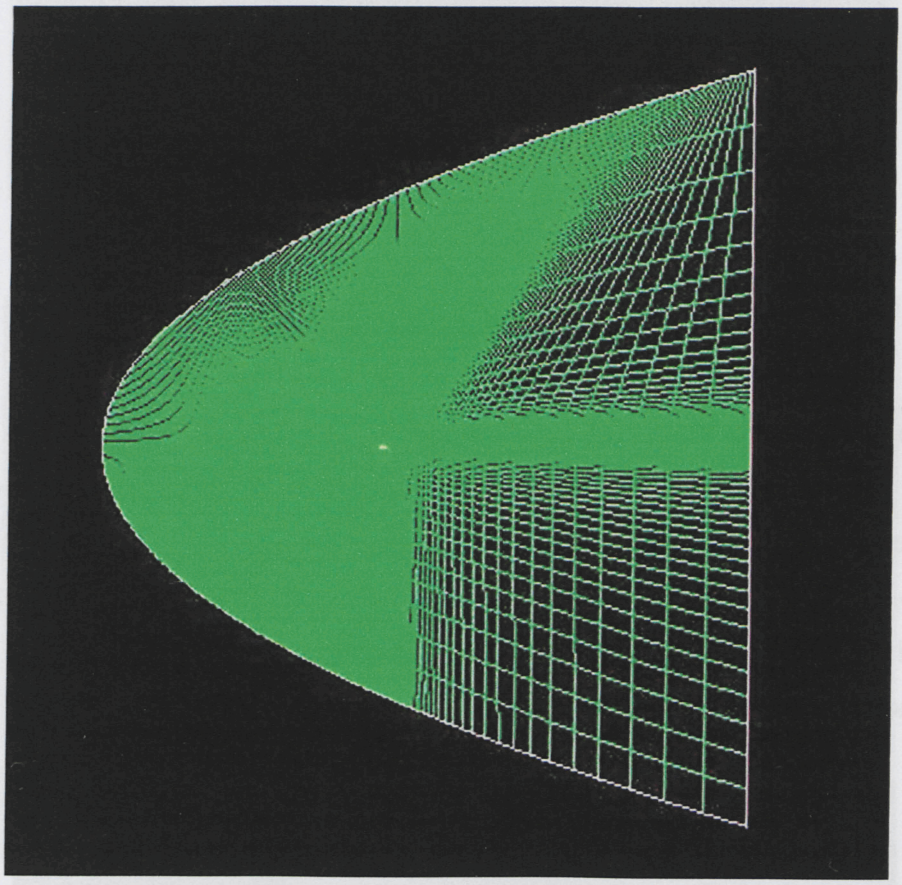

Figure 13: Computational Grid Domain for the Boeing 717 High-Lift System Airfoil

The close-up of the bute-vane-flap region of the computational grid for the base case is shown below in Figure 14. The base case is the current bute-vane-flap configuration on the Boeing 717, where the bute is deflected at an angle of 35.45° and is approximately 0.17m in length. In order to adequately resolve the viscous effects on the lower surface of the airfoil and the bute, the grid is carried over to the bottom surface of

the spoiler. However, it is also necessary to appropriately resolve the viscous region of the spoiler. It was therefore necessary to ensure that the interaction of the grid zones accommodate this requirement.

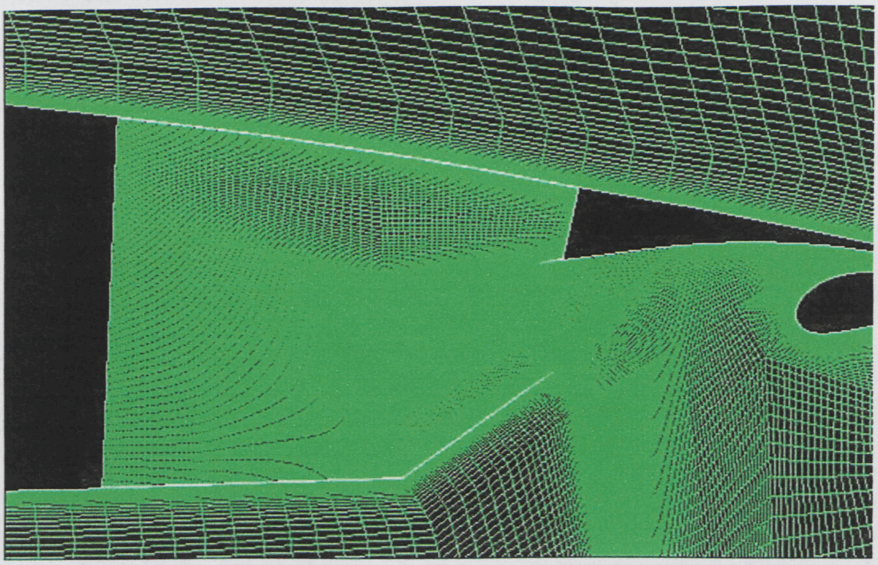

Figure 14: Grid for the Boeing 717 High-Lift System (Base Case)

The other four cases under consideration, the ½ length, the ¾ length, the 25.45° deflection and the 45.45° deflection of the bute, are similar to the base case. However, the change in the bute geometry required a change in the grid density to account for the need to appropriately resolve the viscous regions on the lower surface of the airfoil and bute and the bottom surface of the spoiler. The close-up views of the bute-vane regions for the other four cases are shown below in Figure 15 through Figure 18.

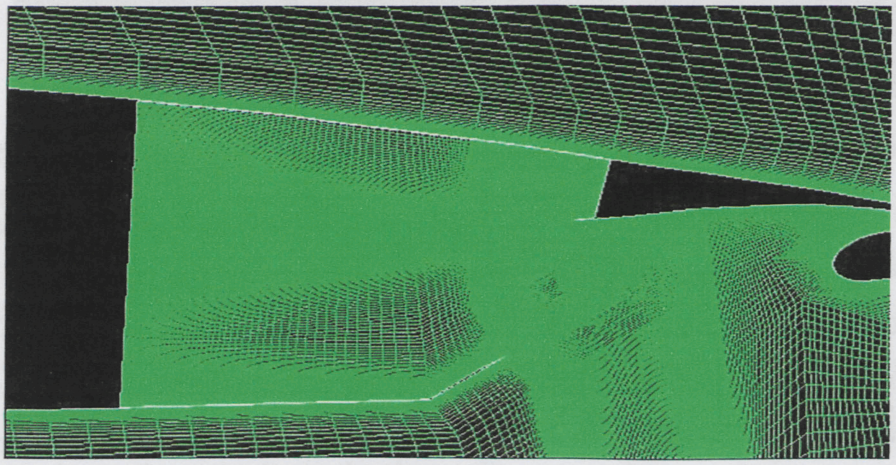

Figure 15: Grid for the Boeing 717 High-Lift System (Bute of Half Length)

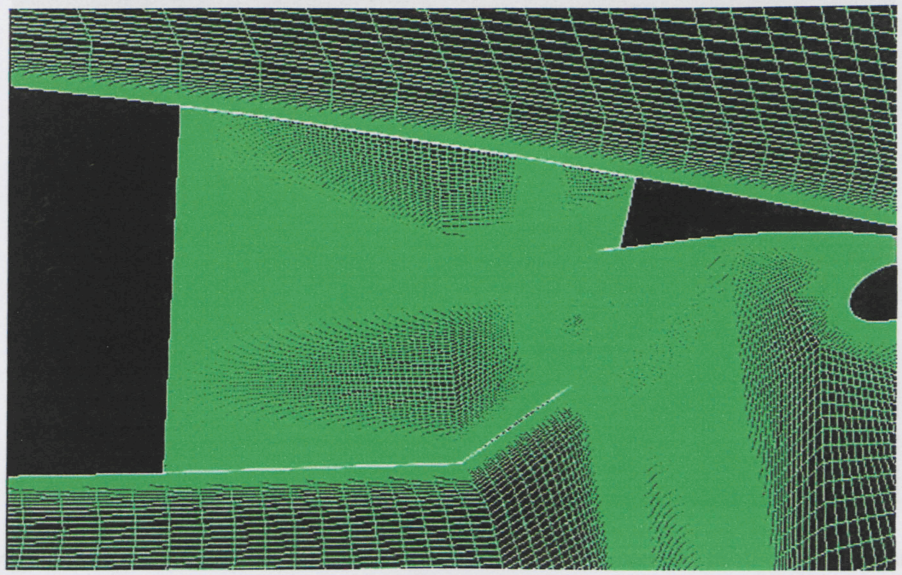

Figure 16: Grid for the Boeing 717 High-Lift System (Bute 3/4 Length)

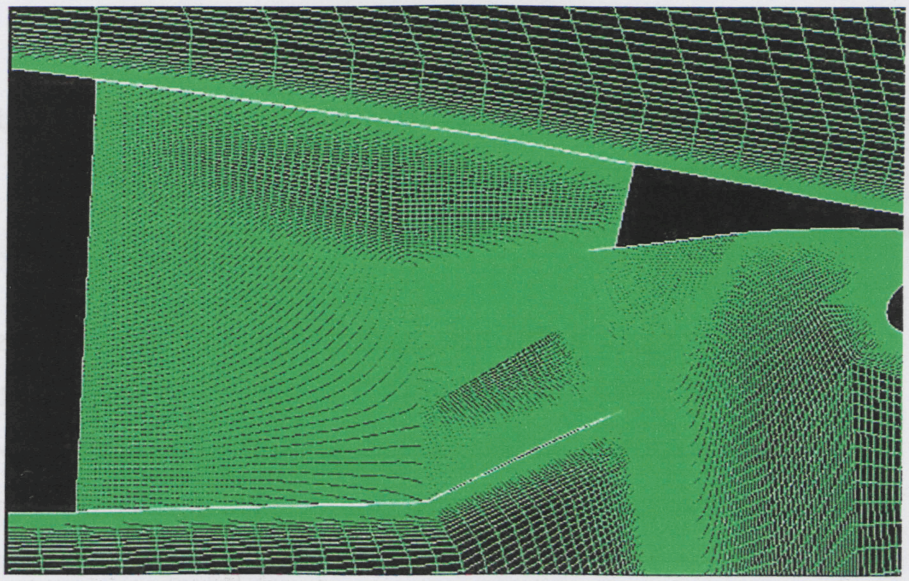

Figure 17: Grid for the Boeing 717 High-Lift System (Bute Deflection of 25.45 Degrees)

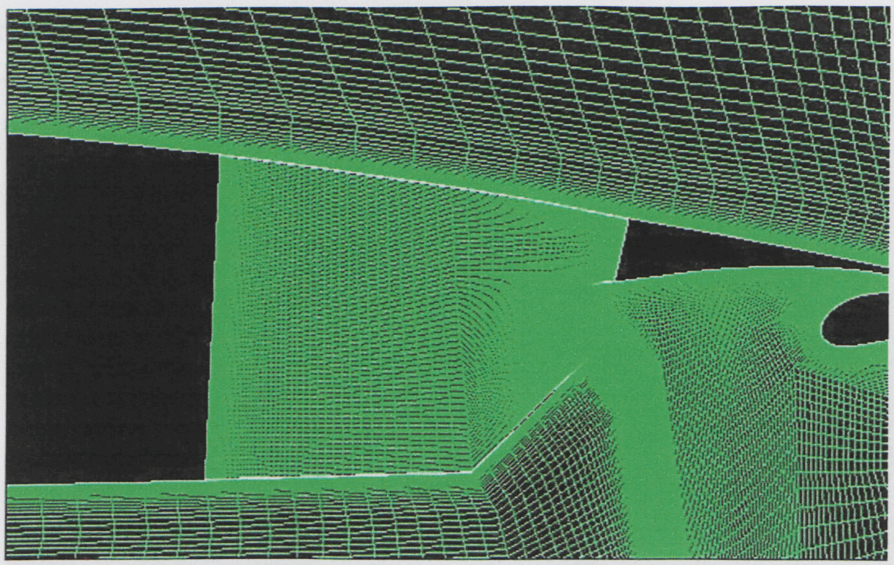

Figure 18: Grid of the Boeing 717 High-Lift System (Bute Deflection of 45.45 Degrees)

2.4 Grid Boundary Conditions

With the mesh generated, it was then necessary to assign appropriate boundary conditions to the elements so that the grid could be exported to FLUENT. The boundaries assigned for all cases analyzed were:

1. All edges forming the airfoil, bute, spoiler, vane, and flap were classified and designated as WALL in GAMBIT. The WALL boundary condition was chosen, as it represents the bounds between the fluid and solid regions of the grid. Since viscous effects are under consideration in this project, the no-slip boundary condition was enforced on these WALL boundaries, such that the velocity at the wall is zero with adiabatic conditions.
2. All edges forming the far-field boundary were classified and designated as PRESSURE-FAR-FIELD in GAMBIT. The PRESSURE-FAR-FIELD boundary condition was chosen as it is non-reflective and it models free stream compressible flow at infinity. The non-reflective nature of the PRESSURE-FAR-FIELD boundary allows waves to pass through the boundaries without spurious reflections; as such, reflections can negatively affect the convergence rate.

3. All other edges were classified and designated as INTERNAL in GAMBIT. This classification of the remaining interior edges as INTERNAL treats these edges as if they were not there (i.e., allowing the data to read across these edges as if the edge did not exist). This allows for faster computational times and thus the grid is more efficient.

CHAPTER 3: CFD ANALYSIS

3.1 Introduction

All CFD analysis codes reduce the governing discretized Navier-Stokes equations into linear algebraic equations that numerically solve the flow field. In this project, since turbulent flow is expected, an additional equation that models turbulence must also be included. These discretized equations are then solved for each cell of the computational domain (grid). The accuracy of the solution is therefore highly dependent on the grid spacing of the mesh. As mentioned in the previous chapter, regions with high gradients, such as the boundary layer region, require very fine grid spacing (i.e., very small control volumes) to accurately capture these phenomenon. The CFD software package used to carry out the analysis was FLUENT.

All the FLUENT analyses performed, were carried out following these steps. First, the grid was imported, loaded, and checked for errors (most notably for negative control volumes). With the grid-check completed, the appropriate models and parameters for the analysis were set. The solution was then iterated until convergence was achieved. With the solution process completed, the post-processing analysis, the collecting of data and plots were carried out. The following sections describe and discuss the analysis set up in detail.

3.2 Setting Up the Analysis

3.2.1 Flow Solver

The COUPLED-IMPLICIT solver was chosen. The implicit solver was chosen because it is less restrictive in maximum time step size than an explicit formulation. The implicit solver requires more memory allocation than an explicit solver; however, for two-dimensional (2D) cases, memory requirement is not an issue.

The STEADY-STATE solution was used. For steady state conditions if flow is entering the trailing edge cavity, then it must also leave the cavity to satisfy continuity. Therefore, the steady-state results will only give a qualitative indication of the flow field configuration given the problem parameters. It cannot be relied on to quantitatively estimate the total mass flow for a specific period, such as over a single take-off or landing sequence.

3.2.2 Energy

The ENERGY equation was used to allow for compressible effects. An equation of state was used to determine the local pressure as a function of density, energy, and velocity.

3.2.3 Viscous Model

FLUENT offers numerous viscous models; the SPALART-ALLMARAS turbulence model was chosen. The SPALART-ALLMARAS model is a relatively simple 1-equation model that solves a modeled transport equation for kinematic eddy viscosity. This model was specifically designed for aerospace applications involving wall bounded flows and it has been shown to give good results for boundary layers subject to adverse pressure gradients [10]. The default parameters for the SPALART-ALLMARAS model were maintained.

3.2.4 Materials

The material chosen was air, as it is the working fluid for this project. The parameters for air were set as follows

- Density (kg/m^3) → IDEAL-GAS LAW. The working fluid is considered an ideal gas to allow for compressibility.
- C_p (J/kg•K) → 1006.43. This value was kept constant, as the temperature gradients are small enough to be modeled as such.
- Thermal Conductivity (W/m•K) → 0.0242. This parameter was kept constant, again because the temperature gradients are small enough to be modeled as such.
- Viscosity → SUTHERLAND LAW. This model was chosen, as it is a widely used formula for the determination of the viscosity of air for viscous flows. The default parameters for the SUTHERLAND LAW model were maintained.
- Molecular Weight (kg/kmol) → 28.966. This parameter was kept constant, as it is a set value for air.

3.2.5 Operating Conditions

The operating pressure was set to 101325 Pa.

3.2.6 Boundary Conditions

The boundary conditions were set at the PRESSURE-FAR-FIELD boundary, which include pressure, airspeed, temperature, and angle of attack, α. They were set as follows:

- Gauge Pressure (Pa) → 0.

- Mach Number → For the validation cases, the Mach number was set according to the Reynolds number under investigation (R_e=3*10^6→M=0.14, R_e=6*10^6→M=0.28, R_e=9*10^6→M=0.42). For the Boeing 717 High-Lift Airfoil cases, it was set to 0.28.
- Temperature (K) → 300.
- X-Component of Flow Direction → This was assigned values according to the angle of attack under consideration, specifically the cos(α) component.
- Y-Component of Flow Direction → This was assigned values according to the angle of attack under consideration, specifically the sin(α) component.
- Turbulence Specification Method → Modified Turbulent Viscosity
- Initial Turbulent Viscosity → 0.001

3.2.7 Reference Values

In order to obtain the appropriate force coefficients, C_L and C_D, reference values for the airfoil had to be set. For the validation cases, the NACA0012 Plain Airfoil and the NACA0012 Split Flap, the dimensions for the airfoil were set as follows:

- Chord Length (m) → 0.93887
- Depth (m) → 1
- Area (m^2) → 0.93887

For the Boeing 717 high-lift airfoil cases, the dimensions for the airfoil were set as follows:

- Chord Length (m) → 3.9
- Depth (m) → 1
- Area (m^2) → 3.9

All the other reference values (density, temperature, velocity, viscosity) were referenced to the far-field boundary.

3.3 Running the Solution

Once the proper models, boundary conditions, and parameters were set, the solution parameters and the convergence parameters needed to be set. With the solution and convergence parameters set, the solution was then initialized. In the sections below, the setting of the solution and convergence parameters will be discussed.

3.3.1 Solution Controls

In FLUENT, one can set solution controls for the Courant Number, for the under-relaxation factors, and discretization of the governing equations. The analysis of multi-element airfoils is much more unstable than the analysis of simple (plain) airfoil shapes, as FLUENT must solve the multiple boundary layers and the mixing of these boundary layers. With this in mind, the solution controls were set as follows:

- Courant Number → 0.1. The Courant Number was initially set to this value of 0.1. For the validation cases, every 100 iterations, it was increased by 0.1, up to a maximum value of 3.5. For the Boeing 717 High-Lift Airfoil cases, every 100 iterations, it was increased by 0.1, up to a maximum value of 2.5. This allowed the solution to stabilize at the beginning of the simulation.
- Under-Relaxation Factors
  - Modified Turbulent Viscosity → 0.8. Larger under-relaxation values result in faster convergence but instability can arise that may need to be eliminated by decreasing the under-relaxation factors. Due to this fact, the value of 0.8 was chosen, as it was deemed as a compromise between stability and quick convergence.
- Discretization → Second Order Upwind. The second order upwinding scheme was chosen to discretize the governing equations, as it is second order accurate in space.

3.3.2 Convergence Monitors

The solution was assumed to be converged when the residuals for all the equations of motion dropped below or were close to the convergence criteria of $1*10^{-4}$, as any further iteration would not significantly change the solution [10]. The C_L and C_D values were also monitored to ensure that they achieved a fixed value.

3.3.3 Initialization

The solution was then initialized with respect to the far-field boundary. The solution was iterated until convergence was achieved.

3.4 Post-Processing Analysis

Once the solution had converged, the results were easily obtained from graphs and contour plots. The main objectives of this study, the determination of recirculation zones and the entrainment of flow in the trailing edge cavity can be achieved via the contours of density, pressure and velocity, as well as pathlines, to illustrate the flow field for each case. How these two factors, recirculation and entrainment, affect the aerodynamic performance can also be determined from the C_L and C_D values and the pressure distribution over the lifting surfaces for each case.

3.5 Y+ Values

Once the solution is obtained it is important to check the distribution of the y+ values over the lifting surfaces. The y+ values are dependent on the resolution of the grid (the off-wall spacing of the grid). These values indicate, at the point in question, the characteristics of the turbulent boundary layer. The y+ values of the nearest grid points to the solid wall should be as low as possible, to achieve the greatest accuracy. For the Spalart-Allmaras model used, it is suggested that the y+ value equal 1 or approximately

30 or greater [10]. If the y+ value is on the order 1 for the first off-wall node for the Spalart-Allmaras model, the viscous sublayer of the turbulent boundary layer is characterized. If the y+ value is 30 for the Spalart-Allmaras model, the log-law model is employed to characterize the boundary layer. For the NACA0012 Plain Airfoil case, y+ values on the order of one were obtained. However, for the more complex geometry associated with high-lift devices, y+ values on the order of one were not attainable, as issues arose with off-wall spacing in the grid generation process. Therefore, for the solutions pertaining to high-lift devices, the y+ values are as low as possible, while still providing a converged solution. For these cases, the y+ distribution over the lifting surfaces was kept on the order of ten over the entire configuration, which is in fair agreement with the constraints of the Spalart-Allmaras model.

CHAPTER 4: VALIDATION OF CFD SOFTWARE

4.1 Introduction

Before using FLUENT to analyze the Boeing 717 high-lift system, it was necessary to establish that FLUENT would generate valid results. As mentioned previously, the NACA0012 plain airfoil and the NACA0012 Split Flap airfoil were used as validation cases. The NACA0012 plain flap was used to ensure that an increase in Reynolds number would not affect the accuracy of the results. The NACA0012 Split Flap was used to validate that indeed FLUENT could generate accurate results for airfoils with high-lift devices deployed. The following sections present the results of the various cases used to validate FLUENT.

4.2 NACA0012 Plain Airfoil

The flow field over the NACA0012 plain airfoil was simulated under three conditions, for Reynolds numbers of $3*10^6$, $6*10^6$, and $9*10^6$. For each of the three conditions, several angle of attacks were used. The numerical results obtained by

FLUENT were then compared to the published data found in Abbot and Von Doehoff's *Theory of Wing Sections*, [1]. The results and comparison for each case are provided below.

4.2.1 Results for Case 1: Reynolds Number $3*10^6$

In Table I, found below, the results obtained by the FLUENT analysis for the NACA0012 plain airfoil for a Reynolds number of $3*10^6$ and those found in literature are presented. The percent error between the numerical (FLUENT) analysis and experimental data is also presented in Table I. From Table I, it can be seen that in general the percent error is approximately within 15%. With the percent error within the range of 15%, typically the value at which results are considered accurate, FLUENT was considered to have produced numerically accurate results for this case.

Table I: Case 1 Results for $R_e=3*10^6$

	FLUENT ANALYSIS		PUBLISHED DATA		PERCENTAGE ERROR	
AOA	C_L	C_D	C_L	C_D	C_L	C_D
-5	-0.57	0.012	-0.53	0.013	7.55	7.69
-3	-0.3	0.011	-0.3	0.011	0.00	0.00
-2	-0.2	0.01	-0.2	0.01	0.00	0.00
0	. 0	0.0108	0	0.0097	0.00	11.34
2	0.23	0.0112	0.23	0.0103	0.00	8.74
5	0.57	0.012	0.55	0.013	3.64	7.69
10	1.1	0.015	1.1	N/A	0.00	N/A
15	1.3	0.033	1.5	N/A	13.33	N/A

4.2.2 Results for Case 2: Reynolds Number $6*10^6$

The results obtained by FLUENT for the Reynolds number case of $6*10^6$, the published data from the literature and the percent error between the two are presented below in Table II. For this case, the percent error is also within the range of 10%; therefore, the numeric results are considered accurate.

Table II: Case 2 Results for $R_e=6*10^6$

	FLUENT ANALYSIS		PUBLISHED DATA		PERCENTAGE ERROR	
AOA	C_L	C_D	C_L	C_D	C_L	C_D
-5	-0.60	0.012	-0.53	0.013	13.21	7.69
-3	-0.36	0.010	-0.32	0.011	12.50	9.09
-2	-0.25	0.01	-0.23	0.01	8.70	0.00
0	0	0.0096	0	0.0097	0.00	1.03
2	0.24	0.0097	0.23	0.0103	4.35	5.83
5	0.60	0.011	0.55	0.013	9.09	15.38
10	1.1	0.018	1.1	N/A	0.00	N/A
15	1.4	0.041	1.5	N/A	6.67	N/A

4.2.3 Results for Case 3: Reynolds Number $9*10^6$

In Table III below, the results obtained from the FLUENT analysis for the NACA0012 plain airfoil for a Reynolds number of $9*10^6$ and the experiment data found in literature are presented. The percent error between the results of the FLUENT analysis and experimental data is also presented in Table III. It can be seen that the percent error is generally within 15%.

Table III: Case 3 Results for $R_e=9*10^6$

	FLUENT ANALYSIS		PUBLISHED DATA		PERCENTAGE ERROR	
AOA	C_L	C_D	C_L	C_D	C_L	C_D
-5	-0.63	0.011	-0.55	0.013	14.55	15.38
-3	-0.38	0.010	-0.34	0.011	11.76	9.09
-2	-0.26	0.01	-0.23	0.01	13.04	0.00
0	0	0.0089	0	0.0097	0.00	8.25
2	0.26	0.0093	0.23	0.0103	13.04	9.71
5	0.63	0.011	0.55	0.013	14.55	15.38
10	1.1	0.025	1.1	N/A	0.00	N/A
15	1.0	0.084	1.5	N/A	33.33	N/A

4.3 NACA0012 Split Flap Airfoil

With the results obtained for the three conditions for the NACA0012 plain airfoil and deemed accurate to within 15%, the NACA0012 Split Flap airfoil was analyzed in FLUENT. The Split Flap was analyzed at a Reynolds number of $6*10^6$ and at several angles of attack. The numerical results obtained by FLUENT were then compared to the published data found in reference 1. The results obtained from FLUENT are presented in Table IV, along with the published data and the resulting percent error. From Table IV, it can be seen that the numerical results are in good agreement with the published data, as the percent error is generally within 10%.

Table IV: Results for the NACA0012 Split Flap (60° Deflection) at $R_e=6*10^6$

	FLUENT ANALYSIS		PUBLISHED DATA		PERCENTAGE ERROR	
AOA	C_L	C_D	C_L	C_D	C_L	C_D
-5	0.87	0.16	0.83	N/A	4.82	N/A
-3	1.1	0.15	1.1	N/A	0.00	N/A
-2	1.3	0.05	1.2	N/A	8.33	N/A
0	1.4	0.17	1.4	N/A	0.00	N/A
2	1.5	0.17	1.6	N/A	6.25	N/A
5	2.08	0.14	1.93	N/A	7.77	N/A
10	1.92	0.21	2.37	N/A	18.99	N/A
15	1.7	0.34	1.8	N/A	5.56	N/A

4.4 Discussion

From the above results, it is evident that FLUENT yields accurate results, within 10% generally. The cases where the percent error was 20% or greater, occurred at high angles of attack where the onset of separation is the likely reason for the discrepancy. Since the CFD analysis was in reasonable agreement with the published data, specifically

for the NACA0012 Split Flap airfoil case, the CFD software (FLUENT) was considered validated and thus could be implemented in the analysis of the Boeing 717 high-lift airfoil.

CHAPTER 5: RESULTS AND DISCUSSION

5.1 Results Analysis

For the purpose of analysis and comparison, the original configuration of the trailing edge device of the Boeing 717 high-lift airfoil, with a bute length of 0.17m at an angle of 35.45°, will be considered the base case for all angles of attack under consideration. The angles of attack to be considered are: -5, 0, 5, and 10 degrees. The other four cases analyzed will be compared with this base case with respect to the aerodynamic coefficients, C_L and C_D.

In the analysis, the effect of the entrainment of flow in the flap-well (trailing edge) cavity, if it occurs, will be considered in terms of how it affects the aerodynamic coefficients. In order to determine whether the flow becomes entrained or not, a rake, consisting of 100 points was created at sixty-six percent of the chord length, just before the bute begins. The pathlines of the particles released from the 100 points on the rake were then tracked along the flow field to see if any became entrained. If some of the particles became caught in the flap-well, the length of the rake was adjusted until all 100 particles became entrained. This allowed for the determination of how much of the mass flow is pulled into the trailing edge cavity. The pathlines created by the release of the particles from the rake also allowed for the visualization of the recirculation zones present in the trailing-edge cavity.

5.1.1 Results for the Base Case

Figure 19 below displays the flow field for the base case at $\alpha = -5^{o}$ by providing the contours of velocity magnitude about the airfoil, while Figure 20 illustrates the behaviour of the flow in the trailing edge cavity. As can be seen in Figure 19, the flow on the upper surface remains attached, with the boundary layer growing in thickness as the flow travels downstream. From Figure 20, it can be seen that the high-energy flow from the bottom surface passes through the first slot, between the spoiler and vane, and the second slot, between the vane and flap, to re-energize the boundary layer. The flow is re-engerized just before the main airfoil boundary layer begins to separate, thus preventing separation. From Figure 20, it can also be seen that none of the high-energy flow from the bottom surface becomes entrained in the flap-well and therefore all the high-energy flow is ducted through the two slots.

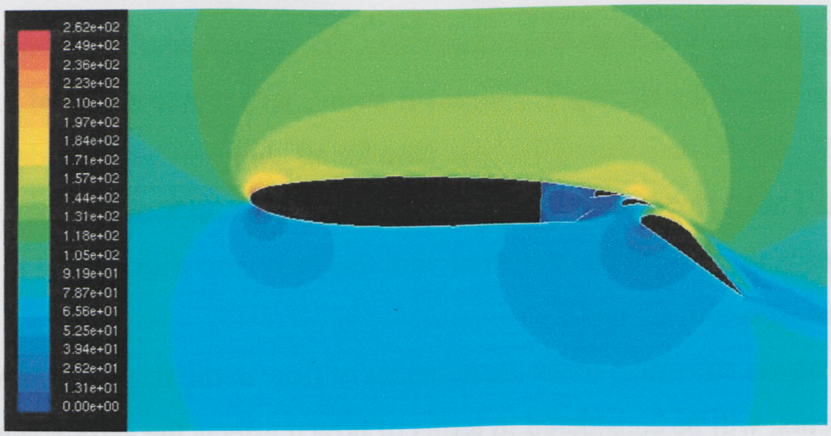

Figure 19: Contours of Velocity Magnitude [m/s], Base Case, α=-5

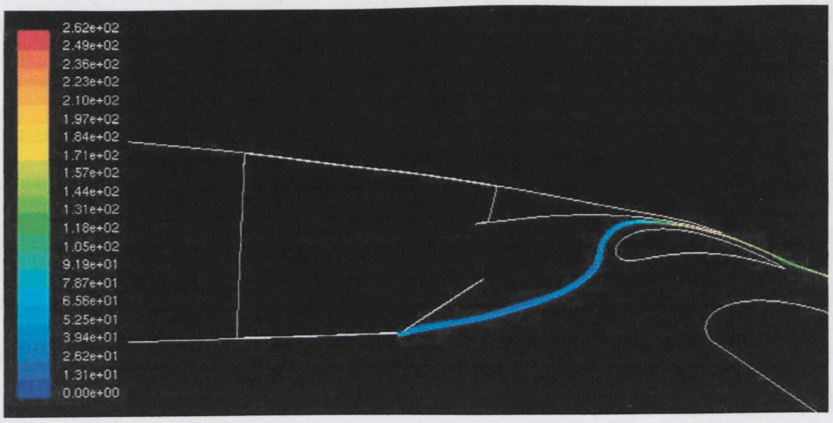

Figure 20: Pathlines Coloured by Velocity Magnitude [m/s], Base Case, α=-5

For the base case at $\alpha = 0^{o}$, Figure 21 illustrates the velocity magnitude contours, which indicate that the flow remains attached on the upper surface. Figure 22 shows that none of the flow is entrained. Therefore, all of the high-energy flow is ducted through the two slots to re-energize the upper surface flow to prevent separation on the top surface of the vane and flap.

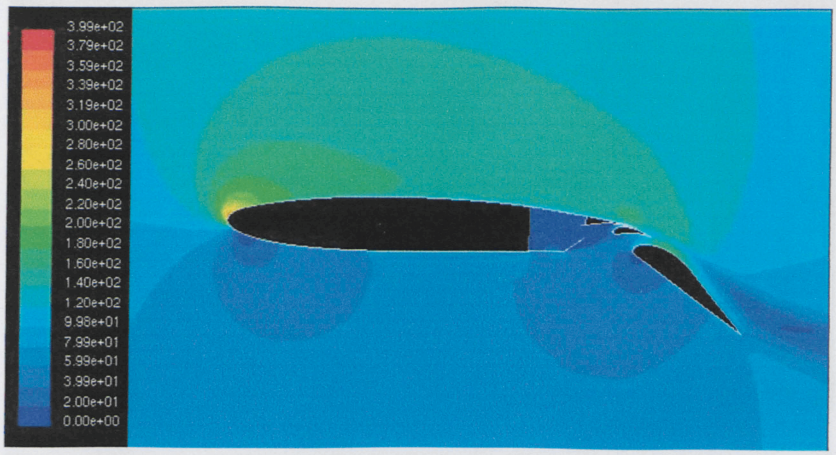

Figure 21: Contours of Velocity Magnitude [m/s], Base Case, α=0

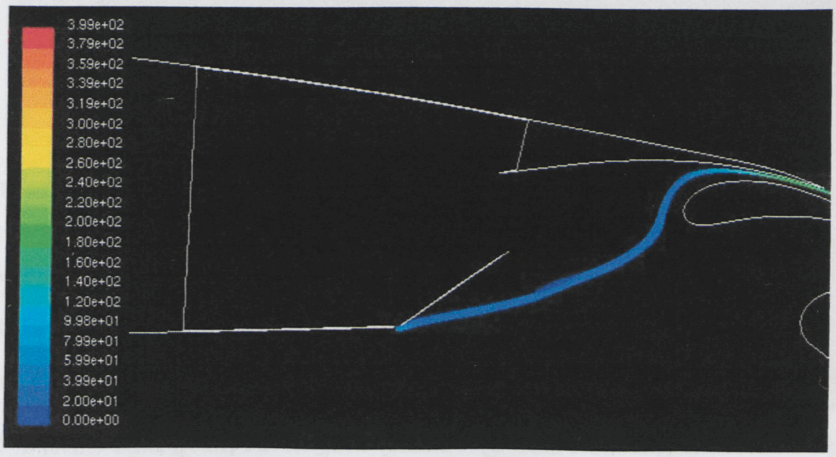

Figure 22: Pathlines Coloured by Velocity Magnitude [m/s], Base Case, α=0

Figure 23 below illustrates the flow field for the base case at $\alpha = 5^{o}$ by providing the contours of velocity magnitude about the airfoil, while Figure 24 displays the behaviour of the pathlines of the flow in the trailing edge cavity. As can be seen in Figure 23, the flow on the upper surface has become detached, and boundary layer separation has occurred. From Figure 24, it can be seen that none of the high-energy

flow is entrained in the trailing edge cavity. It can also be seen that the flow from the bottom surface passes through the second slot, while minimally passing through the first slot. It can also be seen in Figure 24 that the flow that is ducted through the slots flows back over the main airfoil toward the leading edge, indicating that flow separation has occurred.

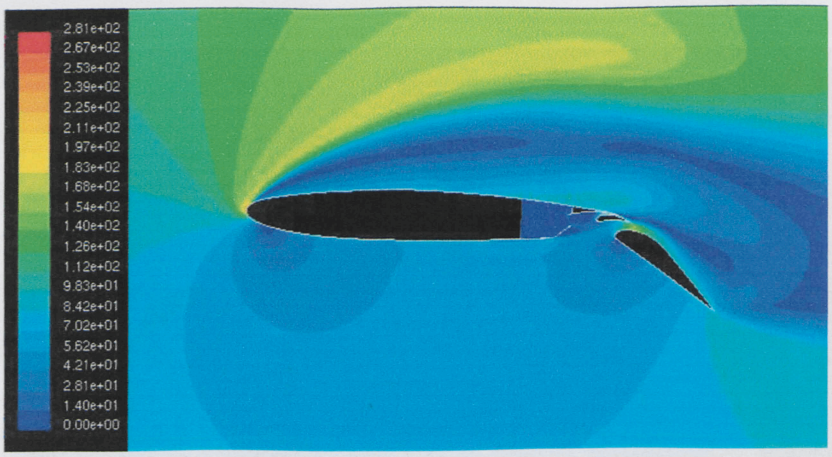

Figure 23: Contours of Velocity Magnitude [m/s], Base Case, α=5

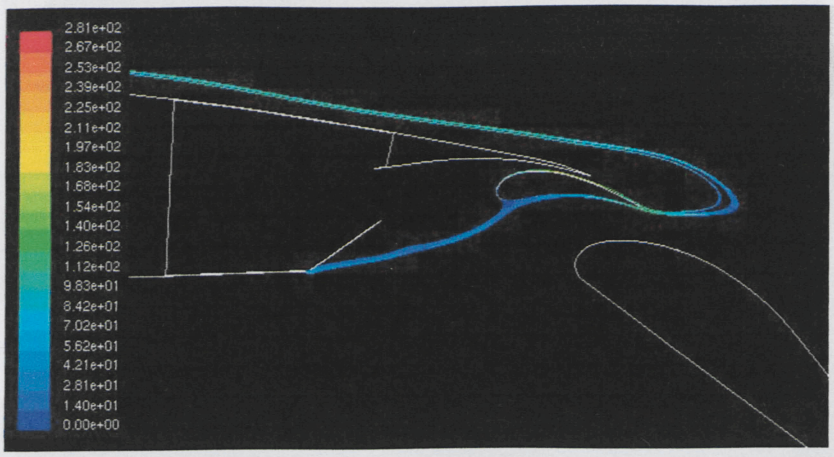

Figure 24: Pathlines Coloured by Velocity Magnitude [m/s], Base Case, α=5

For the base case at $\alpha = 10^{\circ}$, Figure 25 displays the velocity magnitude contours, which indicate that boundary layer separation has occurred. Figure 26, shows that none of the flow is entrained in the trailing edge cavity and that it is only ducted through the second slot, between the vane and flap. From these two figures, it can be seen that the high-energy flow from the bottom surface does not re-energize the upper surface flow, and thus separation occurs.

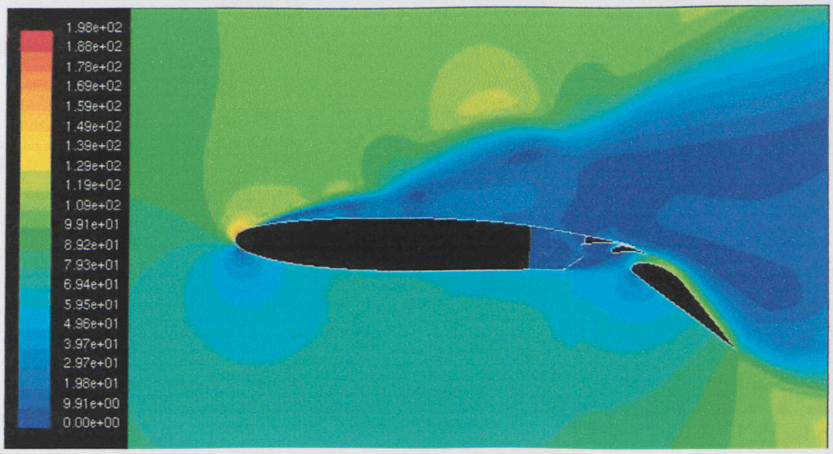

Figure 25: Contours of Velocity Magnitude [m/s], Base Case, α=10

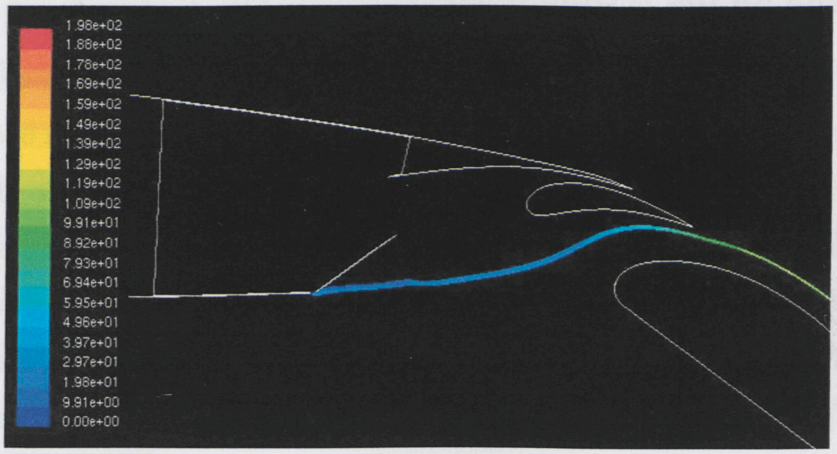

Figure 26: Pathlines Coloured by Velocity Magnitude [m/s], Base Case, α=10

The values obtained by FLUENT for the coefficients of lift and drag for all angles of attack considered for this case are tabulated below in Table V, along with the value for the entrainment mass flow rate. The coefficient of pressure plot and the contours of static pressure for each angle of attack are provided in the Appendix to complement the analysis. As would be expected, when separation occurs C_D increases significantly, since pressure recovery at the trailing edge is incomplete. The large wakes created by the flow separation at the angles of attack of 5 and 10 degrees can be seen in Figures 23 and 25 respectively. From Table V, it is also shown that, at $\alpha=5^o$, the coefficient of lift is at a very high value with a correspondingly high coefficient drag, indicative of the onset of

separation. From Figures 19, 21, 23, and 25, and as tabulated in Table V, it can also be seen that no mass was entrained in the trailing edge cavity at any angle of attack, α.

Table V: Results for the Base Case of the Boeing 717 High-Lift Airfoil

AOA	C_L	C_D	L/D	ENTRAINED MASS FLOW (kg/s per meter length)
-5	2.377772	0.041188	57.73	0
0	2.622430	0.055912	46.9	0
5	2.677415	0.445009	6.017	0
10	0.831636	0.251057	3.313	0

5.1.2 Results for the ½ Bute Case

First, the results for the ½ bute case that were similar to the base case in terms of entrainment will be discussed in general. The cases for which entrainment occurred will be discussed in detail below. For the ½ bute case at $\alpha = 0^o$ and $\alpha = 10^o$, for which there was no entrainment, there was an increase in C_L, in comparison to the base case. In general, the increase in C_L can be attributed to more high-energy flow being ducted through the first slot passage created by the spoiler and vane. For $\alpha = 0^o$, there was a decrease in C_D, and again this is attributed to the fact that more flow passes through the first slot passage. For $\alpha = 10^o$, there was an increase in C_D, which is due to the fact that there is reversed flow, causing circulation zones downstream of the airfoil that create a large wake, as shown in Figures 27 and 28 below.

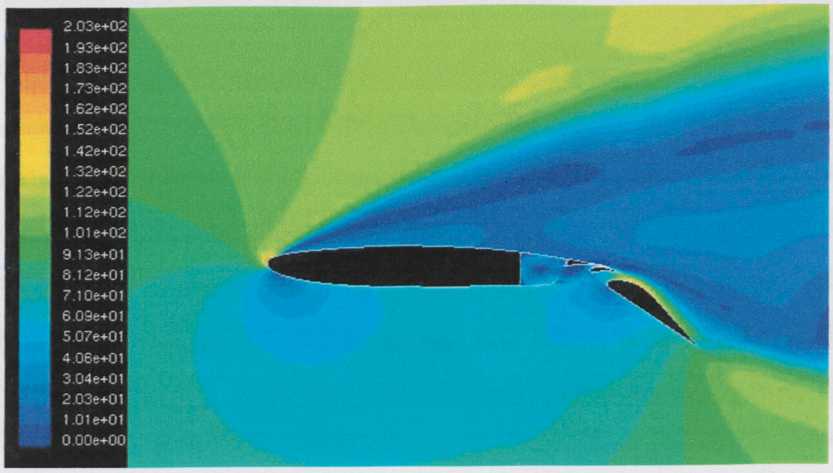

Figure 27: Contours of Velocity Magnitude [m/s], ½ Bute Case, α=10

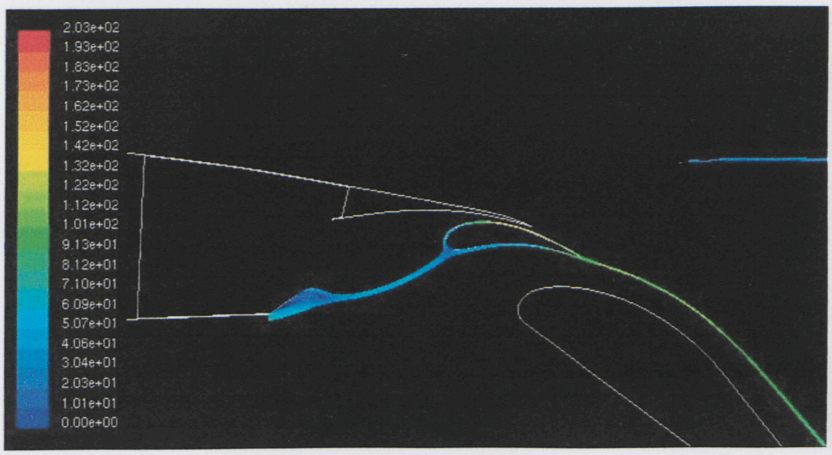

Figure 28: Pathlines Coloured by Velocity Magnitude [m/s], ½ Bute Case, α=10

Entrainment for the ½ bute case occurred at $\alpha = -5^{\circ}$ and $\alpha = 5^{\circ}$. Figure 29 below displays the flow field for the ½ bute case at $\alpha = -5^{\circ}$ by providing the contours of velocity magnitude about the airfoil, while Figure 30 illustrates the behaviour of the flow in the trailing edge cavity. As can be seen in Figure 29, the flow on the upper surface remains attached, with the boundary layer growing in thickness as the flow travels downstream. From Figure 30, it can be seen that the high-energy flow from the bottom surface is entrained in the trailing edge cavity. This stream of flow circulates around the inside of the trailing edge cavity, further energizing the flow that is ducted to the upper surface. The increase in C_L for this angle of attack, in comparison to the base case, is a direct result of the entrainment.

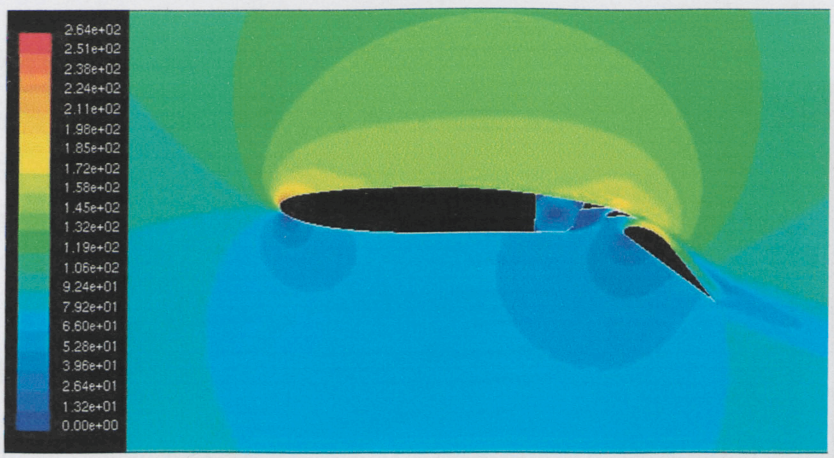

Figure 29: Contours of Velocity Magnitude [m/s], ½ Bute Case, α=-5

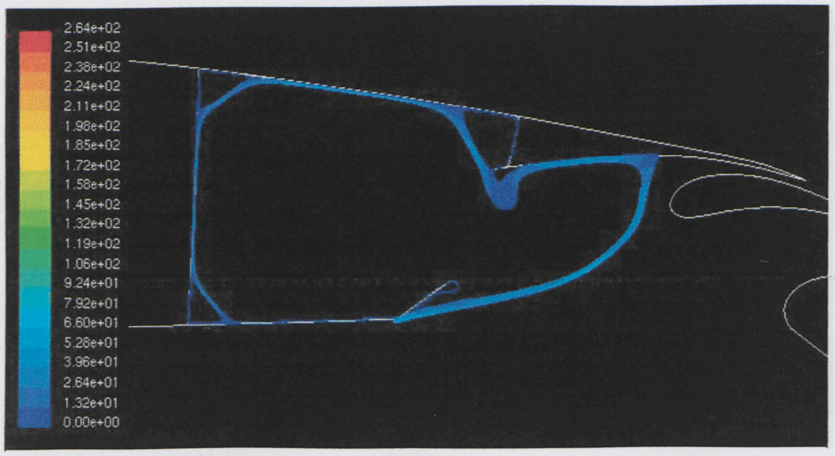

Figure 30: Pathlines Coloured by Velocity Magnitude [m/s], ½ Bute Case, α=-5

Figures 31 and 32 below, illustrate the flow field for the ½ bute case at $\alpha = 5^{o}$ via contours of velocity magnitude and pathlines. As can be seen in Figure 29, a moderate degree of separation has occurred on the upper surface, as indicated by the large wake downstream of the airfoil. From Figure 32, it can be seen that some of the high-energy flow from the bottom surface is entrained in the trailing-edge cavity. This stream of flow circulates around the inside of the trailing edge cavity, depositing contaminants if present in the flow. It can also be seen from Figure 31, that flow over the vane is separated but not so over the flap. The decrease in C_L for this angle of attack, in comparison to the base case, is a result of boundary layer separation. For this case, the wake region is much smaller in comparison to the base case, and therefore, explains why there was a decrease in C_D.

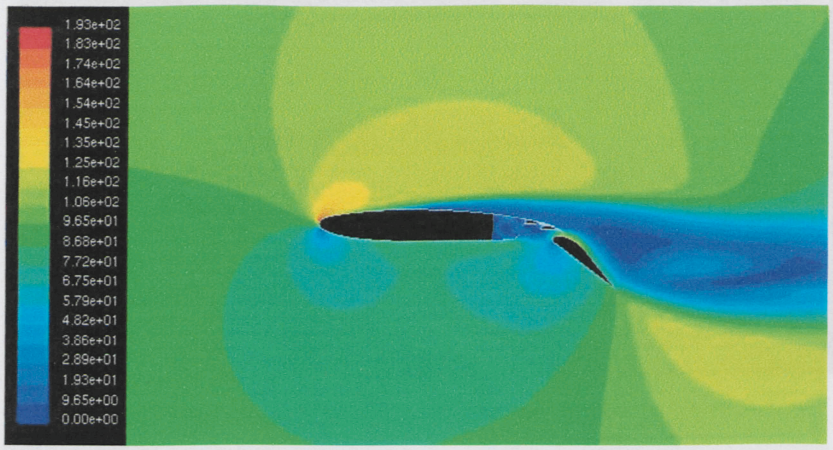

Figure 31: Contours of Velocity Magnitude [m/s], ½ Bute Case, α=5

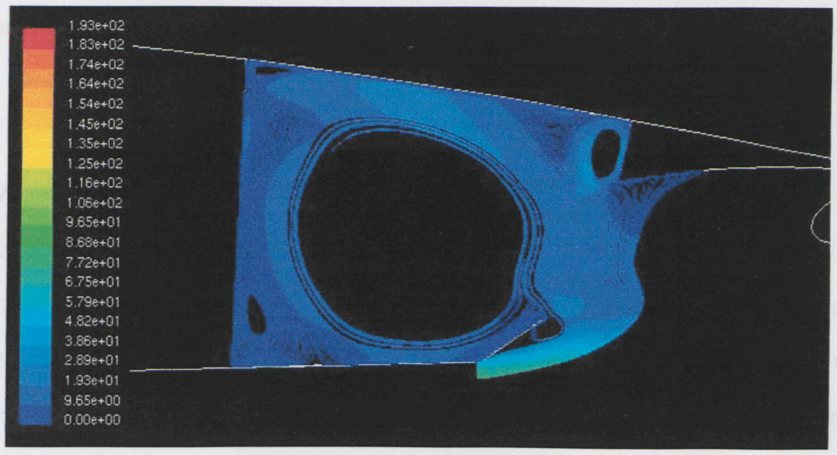

Figure 32: Pathlines Coloured by Velocity Magnitude [m/s], ½ Bute Case, α=5

The values obtained by FLUENT for the coefficients of lift and drag for all angles of attack considered for this case are tabulated below in Table VI. The values for the entrained mass flow are also tabulated in Table VI. The coefficient of pressure plot and the contours of static pressure for each angle of attack are provided in the Appendix to complement the analysis. As expected, based on the above discussion, when separation occurs, C_D increases significantly due to the fact the there is incomplete pressure recovery at the trailing edge. The large wakes created by the flow separation at the angles of attack of 5 and 10 degrees can be seen in Figures 31 and 27, respectively.

Table VI: Results for the ½ Bute Case of the Boeing 717 High-Lift Airfoil

AOA	C_L	C_D	L/D	ENTRAINED MASS FLOW (kg/s per meter length)
-5	2.391110	0.042241	56.61	0.21031
0	2.670572	0.044369	60.19	0
5	1.378644	0.314962	4.377	1.25833
10	1.319928	0.434892	3.035	0

5.1.3 Results for the ¾ Bute Case

For the ¾ bute case at $\alpha = -5^o$ and $\alpha = 0^o$, there was no flow entrainment in the trailing edge cavity, similar to the base case. In comparison to the base case, for angles of attack of -5^o and 0^o, there was an increase in C_L and a decrease in C_D. This is

attributed to the fact that the flow separation occurs farther up the length of the bute, thereby better directing the flow through the first slot between the spoiler and vane where the boundary layer is first re-energized.

At $\alpha = 5^{o}$ and $\alpha = 10^{o}$, for the ¾ bute case, flow becomes entrained. At $\alpha = 5^{o}$, as shown in Figure 33, separation on the upper surface has just occurred, as indicated by the relatively small wake downstream of the airfoil. From Figure 34, it can be seen that some of the high-energy flow from the bottom surface is entrained in the trailing edge cavity. This stream of fluid flow is trapped in the trailing edge cavity and as such does not interact with the flow passing through the first slot. The decrease in C_L for this angle of attack, in comparison to the base case, can be attributed to the boundary layer separation on the upper surface, in conjunction with the entrained flow not further energizing the high-energy flow passing through the spoiler and vane. The decrease in C_D, in comparison to the base case, is a direct result of the extent of boundary layer separation. In this case, boundary layer separation has just occurred and the wake region is relatively small and as such, C_D is not as large.

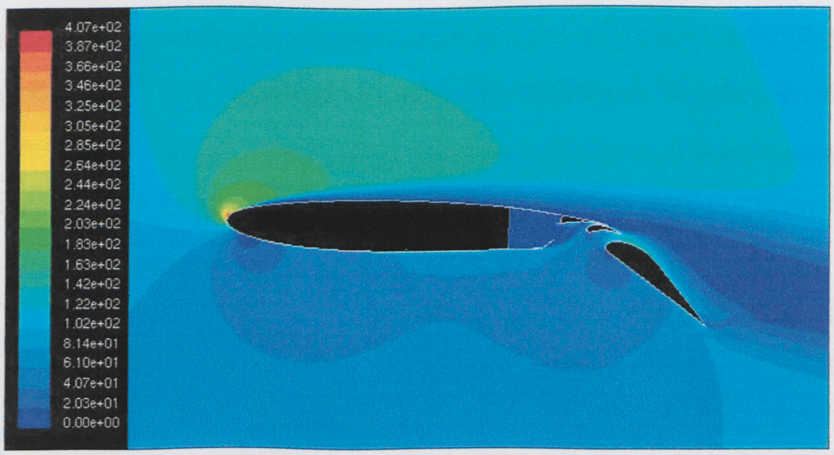

Figure 33: Contours of Velocity Magnitude [m/s], ¾ Bute Case, α=5

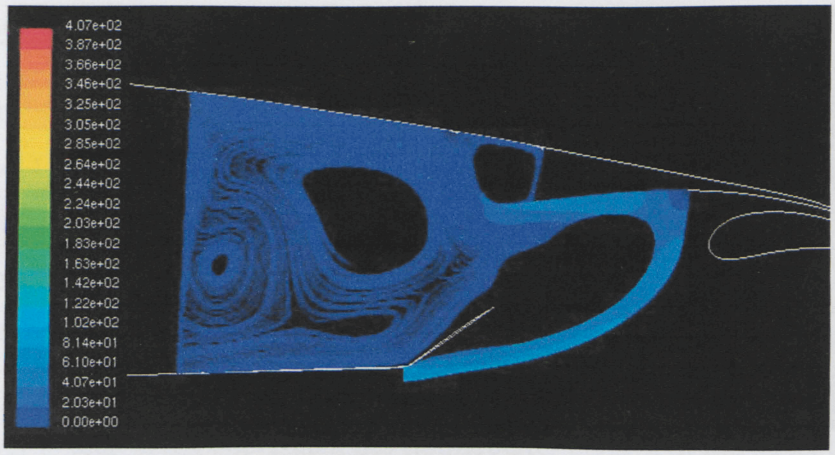

Figure 34: Pathlines Coloured by Velocity Magnitude [m/s], ¾ Bute Case, α=5

Figure 35 below displays the flow field for the ¾ bute case at $\alpha = 10^{o}$ by illustrating the contours of velocity magnitude, while Figure 36 illustrates the behaviour of the flow in the trailing edge cavity. From Figure 35, it can be seen that separation has occurred near the leading edge. From Figure 36, it can be seen that some of the flow is entrained along the bottom of the bute, creating a recirculation zone. The increase in C_L, in comparison to the base case for this angle of attack, is attributed to this recirculation zone. As the fluid flow passes by this zone to flow through the second slot, it is accelerated further, thereby energizing the boundary and controlling the extent of the separation. The increase in C_D, in comparison to the base case for this angle of attack, can be attributed to the boundary layer separation.

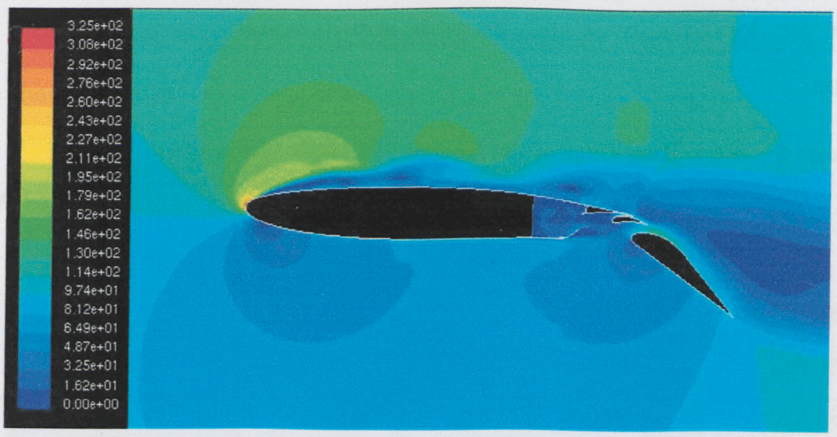

Figure 35: Contours of Velocity Magnitude [m/s], ¾ Bute Case, α=10

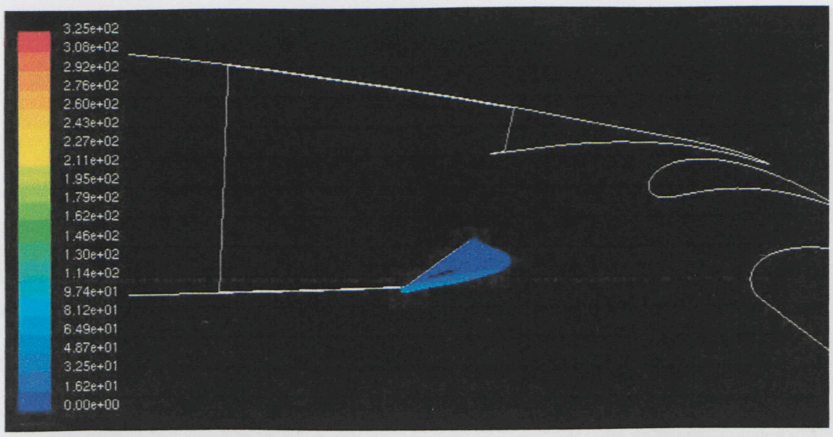

Figure 36: Pathlines Coloured by Velocity Magnitude [m/s], ¾ Bute Case, α=10

The values obtained by FLUENT for the coefficients of lift and drag for all angles of attack considered for this case are tabulated below in Table VII, The values for the entrained mass flow rate are also tabulated in Table VII. To complement the analysis, the coefficient of pressure plot and the contours of static pressure for each angle of attack are provided in the Appendix. As would be expected, when separation occurs C_D increases significantly, since pressure recovery at the trailing edge is incomplete. The wakes created by the flow separation at the angles of attack of 5 and 10 degrees can be seen in Figures 33 and 35, respectively.

In comparing the entrained mass flow rates of the base case, the ½ bute case, and the ¾ bute case, for $\alpha = -5^0$ and $\alpha = 10^o$, if mass is entrained, there is an increase in C_L and C_D in comparison to the base case. For $\alpha = 5^o$, the greater the flow entrainment, the less significant the decrease in C_L and the more significant the decrease in C_D, compared to the base case.

Table VII: Results for the ¾ Bute Case of the Boeing 717 High-Lift Airfoil

AOA	C_L	C_D	L/D	ENTRAINED MASS FLOW (kg/s per meter length)
-5	2.389281	0.037125	64.36	0
0	2.660694	0.051936	51.23	0
5	2.534320	0.292060	8.677	3.88602
10	1.975631	0.351836	5.615	0.49721

5.1.4 Results for the 25.45 Degree Bute Case

The results for the 25.45° bute case, where there was no entrainment will first be discussed and compared to the base case. At $\alpha = -5°$, $\alpha = 0°$, and $\alpha = 5°$, mass was not entrained in the trailing edge cavity. For these three angles of attack, in comparison to the base case, there was an increase in C_L. This can be attributed to the fact that the flow from the bottom surface of the airfoil separates farther up the length of the bute, thereby better directing the flow through the first slot between the spoiler and vane. The boundary layer is thus better energized, providing better control of the onset of separation. For $\alpha = -5°$, and $\alpha = 0°$, there is a decrease in C_D, in comparison to the base case, which is also attributed to the fact that the flow is better directed through the slot passages, thus delaying the onset of separation. However, for $\alpha = 5°$, when compared to the base case, there is an increase in C_D, and this is caused by the reversed flow experienced on the upper surface of the airfoil due to boundary layer separation.

For the 25.45° bute case at $\alpha = 10°$, as illustrated in Figure 38, flow is entrained in front of the entrance to the trailing edge cavity, creating a recirculation zone. This recirculation zone increases the C_L, in comparison to the base case, because as the flow passes by this recirculation zone, the high-energy flow from the bottom surface is further accelerated. With the flow being further accelerated as it passes through the slot passage, the boundary layer is energized, and the extent of separation is controlled. From Figure 37 we can see that separation has occurred at the leading edge of the main airfoil, as well as over both the vane and flap, and thus explains why there is an increase in C_D, when compared to the base case.

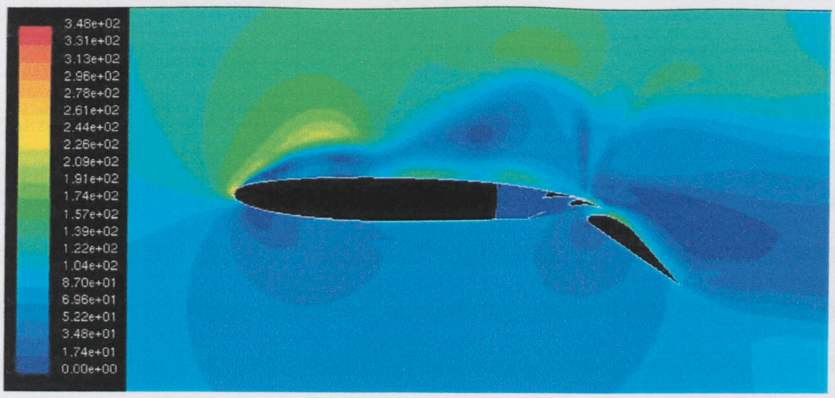

Figure 37: Contours of Velocity Magnitude [m/s], 25.45° Bute Case, α=10

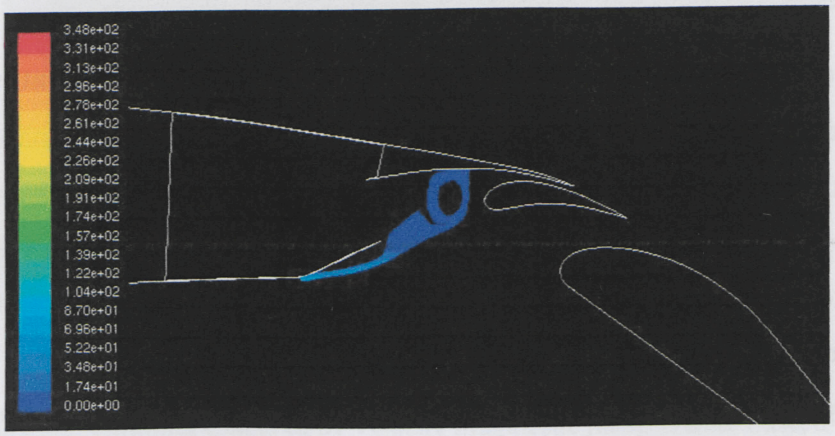

Figure 38: Pathlines Coloured by Velocity Magnitude [m/s], 25.45° Bute Case, α=10

The values obtained by FLUENT for the coefficients of lift and drag for all angles of attack considered for this case are tabulated below in Table VIII, along with the values for the entrained mass flow. In the Appendix, the coefficient of pressure plot and the contours of static pressure for each angle of attack are provided to complement the analysis. Based on the above discussion, when separation occurs, C_D increases significantly as the pressure recovery at the trailing edge is incomplete.

Table VIII: Results for the 25.45 Degree Bute Case of the Boeing 717 High-Lift Airfoil

AOA	C_L	C_D	L/D	ENTRAINED MASS FLOW (kg/s per meter length)
-5	2.38718	0.038712	61.67	0
0	2.680929	0.052644	50.93	0
5	2.829817	0.475118	5.956	0
10	3.013556	0.655402	4.598	0.39116

5.1.5 Results for the 45.45 Degree Bute Case

For the 45.45° bute case, at $\alpha = 0°$, flow is not entrained. There is an increase in C_L and a decrease in C_D in comparison to the base case. This is attributed to the fact that the high-energy flow from the bottom surface of the airfoil is efficiently directed through the first slot passage and thus re-energizes the boundary layer to control separation on the upper surface of the airfoil. For $\alpha = -5°$, $\alpha = 5°$, and $\alpha = 10°$, flow is entrained in the

trailing edge cavity. In comparison to the base case, for the angles of attack of -5° and 5°, there is a decrease in C_L. This decrease is attributed to the earlier separation of the flow along the length of the bute, which directs the bottom surface flow towards the spoiler, instead of toward the slot passage between the spoiler and vane. The entrapped flow in the trailing edge cavity does not interact with the flow from the bottom surface and thus cannot further accelerate the flow through the slot passages. For $\alpha = -5^{\circ}$, there is an increase in C_D when compared to the base case. This is because the boundary layer is not efficiently energized. For $\alpha = 5^{\circ}$, there is a decrease in C_D relative to the base case, due to the fact that the degree of flow separation on the upper surface for the 45.45° case is less extensive. In comparison to the base case, for the angle of attack of 10°, there is an increase in both C_L and C_D. The increase in C_L is again a result of the early separation of the bottom surface flow along the length of the bute better directing the flow through the slot passages and re-energizing the upper surface flow to control the extent of separation. The increase in C_D is a direct result of the greater extent of boundary layer separation.

The values obtained by FLUENT for the coefficients of lift and drag for all angles of attack considered for this case are tabulated below in Table IX, along with the values for the entrained mass flow. The coefficient of pressure plot and the contours of static pressure for each angle of attack are provided in the Appendix to complement the analysis. As discussed above, when separation occurs, C_D increases significantly, since the pressure recovery at the trailing edge is incomplete.

Table IX: Results for the 45.45 Degree Bute Case of the Boeing 717 High-Lift Airfoil

AOA	C_L	C_D	L/D	ENTRAINED MASS FLOW (kg/s per meter length)
-5	2.3658375	0.0447403	52.88	0.09882
0	2.636365	0.0513904	51.3	0
5	2.6617336	0.2604565	10.22	0.92466
10	1.5612521	0.3320969	4.792	0.63044

CHAPTER 6: CONCLUSIONS AND RECOMMENDATIONS

6.1 Conclusions

In conclusion, it has been shown that the CFD software, FLUENT, via simulations for the NACA0012 airfoil at various Reynolds Numbers ($3*10^6$, $6*10^6$, and $9*10^6$) and the NACA0012 60° split flap airfoil ($R_e=6*10^6$) provided numerically accurate results that were generally within 10% of the published experimental data.

It was also found, that as the angle of attack was increased from –5° up to 10°, the recirculation zones within the trailing edge cavity shifted in location and changed in size. For the ½ bute case, with increasing angle of attack, the recirculation zone centered in the trailing edge cavity became more prominent, suppressing the recirculation zones in the corners of the cavity. For the 45.45° bute case, with increasing angle of attack, the central recirculation zone shifted downward toward the bute and reduced in size, while the recirculation zone by the spoiler edge became larger and shifted toward the centre of the cavity.

In this study, it was also determined that mass is indeed entrained depending on the angle of attack, the bute length and bute deflection angle. It was found that when the bute length was changed and entrainment occurred, there was an increase in the lift coefficient for α=-5° and α=10°. It was also found that for these two angles of attack, the

greater the entrainment the greater the improvement in the lift coefficient. For $\alpha=5^{o}$, flow entrainment was detrimental to the lift coefficient. These results are summarized below in Table X.

Table X: Comparison of Flow Entrainment for a Change in Bute Length

	Base Case		½ Bute Case		¾ Bute Case	
AOA	C_L	Entrainment (kg/s•m)	C_L	Entrainment (kg/s•m)	C_L	Entrainment (kg/s•m)
-5	2.377772	0	2.391110	0.21031	2.389281	0
0	2.622430	0	2.670572	0	2.660694	0
5	2.677415	0	1.378644	1.25833	2.534320	3.88602
10	0.831636	0	1.319928	0	1.975631	0.49721

When the bute deflection angle was increased, more mass flow was entrained. For the angles of attack of –5, 0, and 5 degrees, the entrainment impaired the lift qualities of the Boeing 717 wing, suggesting that contaminant entrainment is a detriment to performance for increased bute deflections at these three angles of attack. For the angle of attack of 10 degrees, the entrainment improved the lift coefficient, suggesting that when flow separation has occurred, contaminant entrainment helps to control the separation. When the bute deflection angle was decreased, mass flow was only entrained for $\alpha = 10^{o}$. In this case, the contaminant entrainment was beneficial as it improved the lift coefficient. These results are summarized below in Table XI.

Table XI: Comparison of Flow Entrainment for a Change in Bute Deflection Angle

	Base Case		25.45^{o} Bute Case		45.45^{o} Bute Case	
AOA	C_L	Entrainment (kg/s•m)	C_L	Entrainment (kg/s•m)	C_L	Entrainment (kg/s•m)
-5	2.377772	0	2.38718	0	2.3658375	0.09882
0	2.622430	0	2.680929	0	2.636365	0
5	2.677415	0	2.829817	0	2.6617336	0.92466
10	0.831636	0	3.013556	0.39116	1.5612521	0.63044

Finally, it has been shown that lift and performance of the Boeing 717 wing, have been affected by changing the bute length and the bute deflection angle. By changing the bute length and deflection angle, the high-energy flow from the bottom surface of the airfoil was re-directed. In some cases, some of this flow became entrained in the trailing edge cavity (as noted above), and in others, the flow was directed either toward the slot created by the vane and spoiler or directly toward the lower surface of the spoiler. The case with a bute deflection of 25.45° had the greatest improvement in lift qualities compared to the base case over the range of angles of attack considered and the percent change is tabulated below in Table XII. This is ascribed to the angle of the bute deflection itself, as the high-energy flow from the bottom surface of the airfoil remains attached to the bute over a greater portion of it's length, delaying the separation of the bottom surface flow from the bute. By delaying the separation of the flow from the bute, the flow was more efficiently ducted through both slot passages (of notable importance the slot between the spoiler and vane) for all angles of attacked considered. With the high-energy flow passing through the slot created by the spoiler and the vane, the flow from the upper surface can be re-energized so that the flow over the flap and vane remain attached.

Table XII: Percent Change in Aerodynamic Performance Parameters between the Base and 25.45° Bute Cases

	Base Case			25.45° Bute Case			Percent Change		
AOA	C_L	C_D	L/D	C_L	C_D	L/D	C_L	C_D	L/D
-5	2.377772	0.041188	57.73	2.38718	0.038712	61.67	0.40	-6.01	6.82
0	2.622430	0.055912	46.9	2.680929	0.052644	50.93	2.23	-5.84	8.58
5	2.677415	0.445009	6.017	2.829817	0.475118	5.956	5.69	6.77	-1.01
10	0.831636	0.251057	3.313	3.013556	0.655402	4.598	262.36	161.06	38.81

The bute deflection case of 25.45°, for α=-5°, 0° and 5°, did not have the high-energy flow from the bottom surface of the airfoil entrained in the trailing edge cavity. For α=10°, the bottom surface flow was captured in front of the trailing edge cavity, such that flow was blocked from entering the cavity, thus indicating that entrainment can be beneficial, if the locations of recirculation zones in the trailing edge cavity are known. If the location of recirculation zones can be predicted, the designer or engineer can use

these recirculation zones to improve performance, because if the recirculation zones are appropriately placed in the trailing edge cavity, the high-speed flow from the bottom surface can be further accelerated through the slot passages allowing for greater control of the boundary layer.

The 45.45° bute case was determined to have the worst lift qualities. As mentioned above, this is ascribed to the contaminant entrainment within the trailing edge cavity. For this case, the recirculation zones where located such that the flow from the bottom surface of the airfoil could not be energized by the flow in the recirculation zones. Therefore, the flow impinged on the spoiler instead of being ducted directly through the slot passage between the spoiler and vane and thereby the upper surface boundary layer was not efficiently re-energized, leading to poor lift coefficients in comparison to the other cases, in particular, the base case, as summarized in Table XIII below.

Table XIII: Percent Change in Aerodynamic Performance Parameters between the Base and 45.45° Bute Cases

	Base Case			45.45° Bute Case			Percent Change		
AOA	C_L	C_D	L/D	C_L	C_D	L/D	C_L	C_D	L/D
-5	2.377772	0.041188	57.73	2.3658375	0.0447403	52.88	-0.50	8.63	-8.40
0	2.622430	0.055912	46.9	2.636365	0.0513904	51.3	0.53	-8.09	9.38
5	2.677415	0.445009	6.017	2.6617336	0.2604565	10.22	-0.59	-41.47	69.86
10	0.831636	0.251057	3.313	1.5612521	0.3320969	4.792	91.34	32.28	44.65

6.2 Recommendations

From this study, and the results obtained, several recommendations can be made. First, the ability to determine the streamline that defined complete entrainment lends itself to errors and as such it is recommended that a more accurate method of defining what becomes entrained in the trailing edge cavity be determined and used. Secondly, the contaminant diffusion across the streamlines should also be investigated, as it was beyond the scope of this project. Thirdly, given that eight of the twenty cases analyzed experienced contaminant entrainment and that these analyses were done under steady state conditions, it is recommended that a species concentration analysis be performed to see how the entrained flow behaves over time. Finally, given that higher values of lift

were obtained for the bute deflection angle of 25.45°, it is recommended that the affect of varying airspeeds be investigated to see if indeed this deflection is optimal for all takeoff and landing speeds.

APPENDIX

A.1 Base Case Contour Plots

A.1.1 α=-5

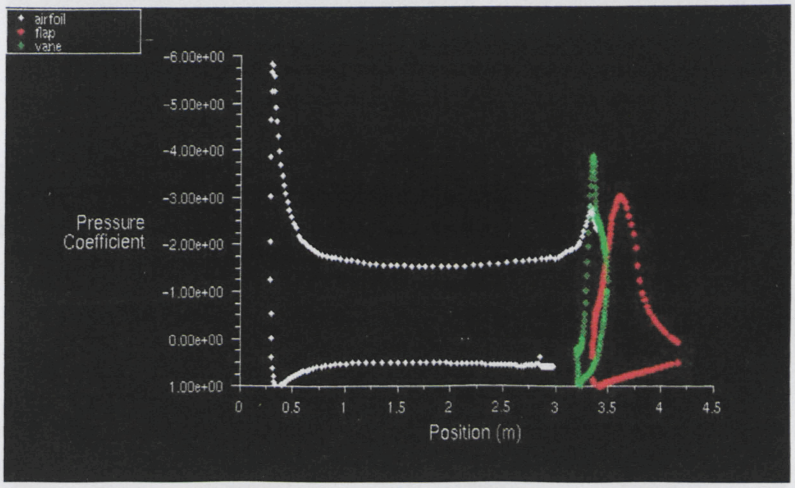

Figure 39: Pressure Distribution over the Lifting Surfaces, Base Case, α=-5

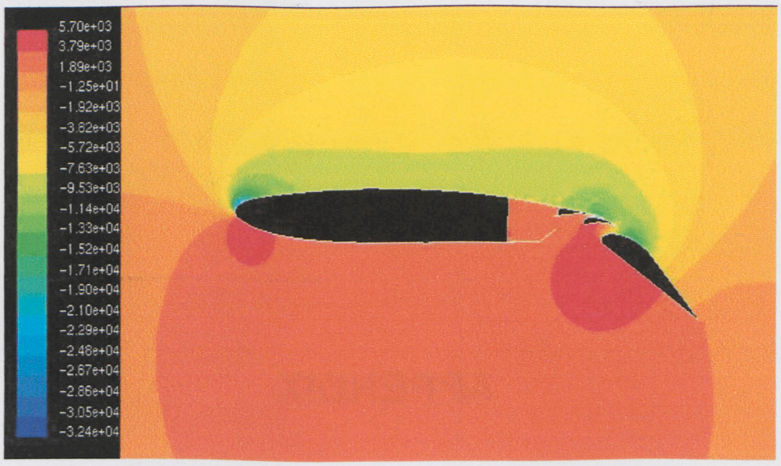

Figure 40: Contours of Static Pressure [Pa], Base Case, α=-5

A.1.2 α=0

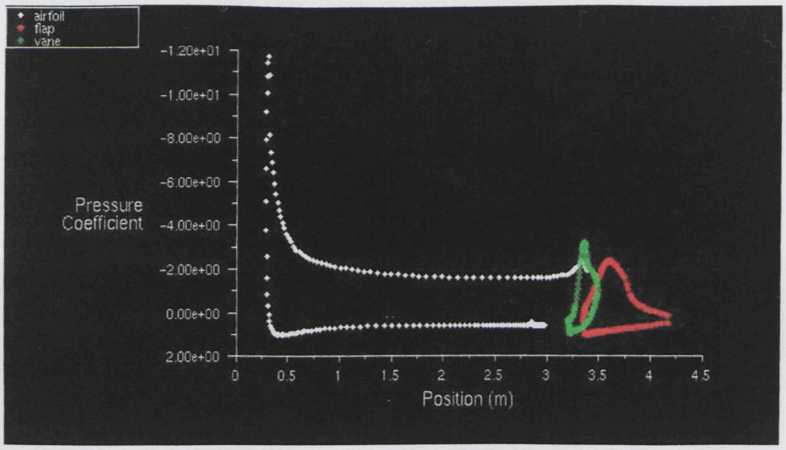

Figure 41: Pressure Distribution over the Lifting Surfaces, Base Case, α=0

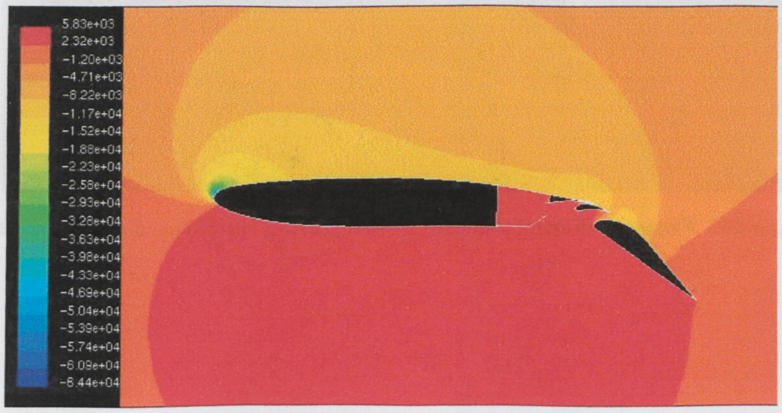

Figure 42: Contours of Static Pressure [Pa], Base Case, α=0

A.1.3 α=5

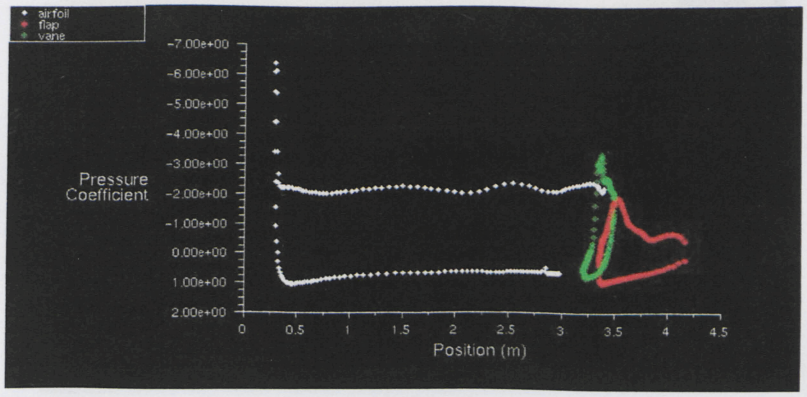

Figure 43: Pressure Distribution over the Lifting Surfaces, Base Case, α=5

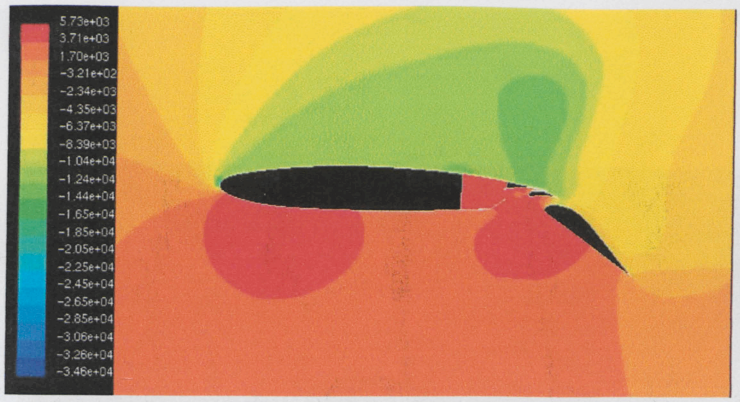

Figure 44: Contours of Static Pressure [Pa], Base Case, α=5

A.1.4 α=10

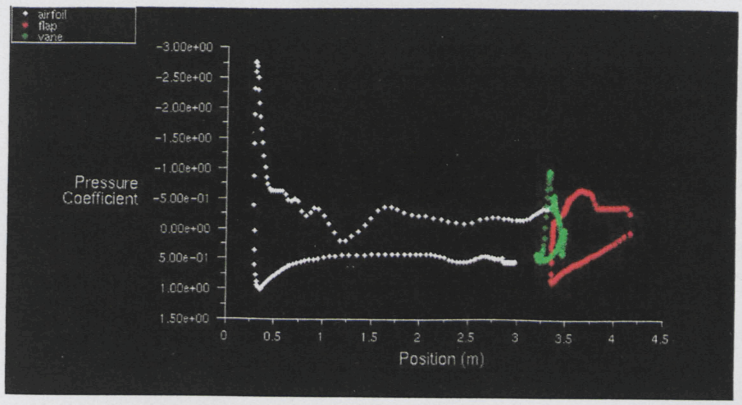

Figure 45: Pressure Distribution over the Lifting Surfaces, Base Case, α=10

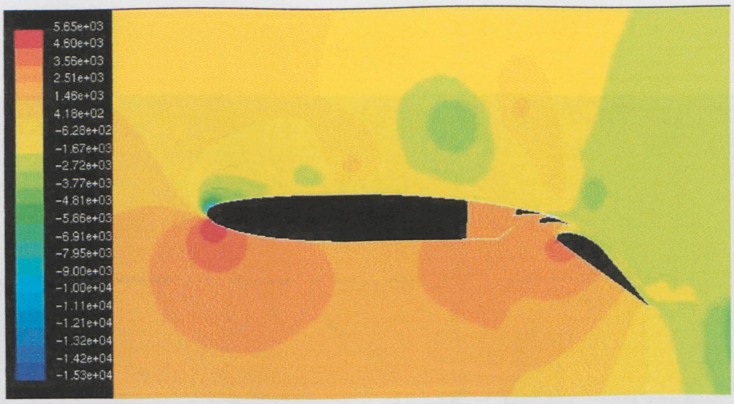

Figure 46: Contours of Static Pressure [Pa], Base Case, α=10

A.2 ½ Bute Case Contour Plots

A.2.1 α=-5

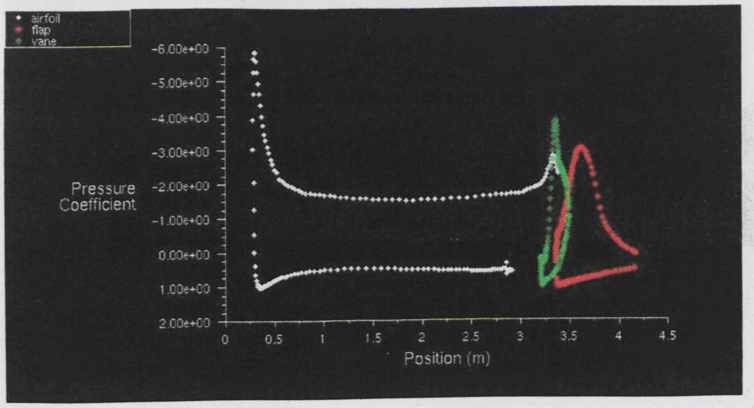

Figure 47: Pressure Distribution over the Lifting Surfaces, Base Case, α=-5

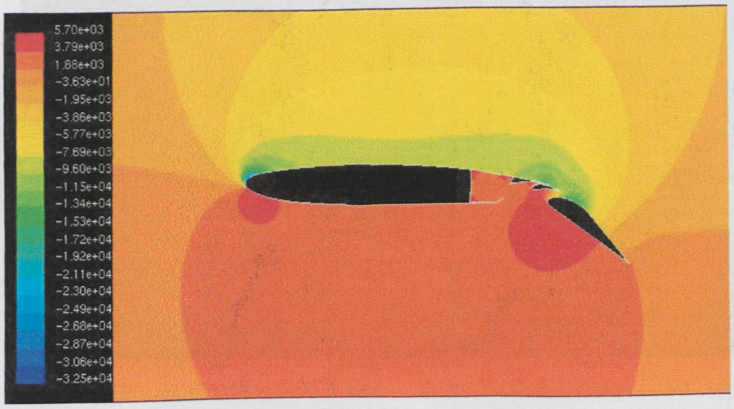

Figure 48: Contours of Static Pressure [Pa], ½ Bute Case, α=-5

A.2.2 α=0

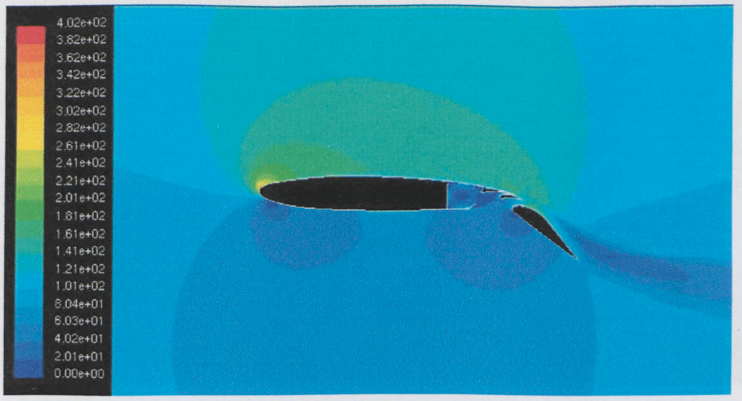

Figure 49: Contours of Velocity Magnitude [m/s], ½ Bute Case, α=0

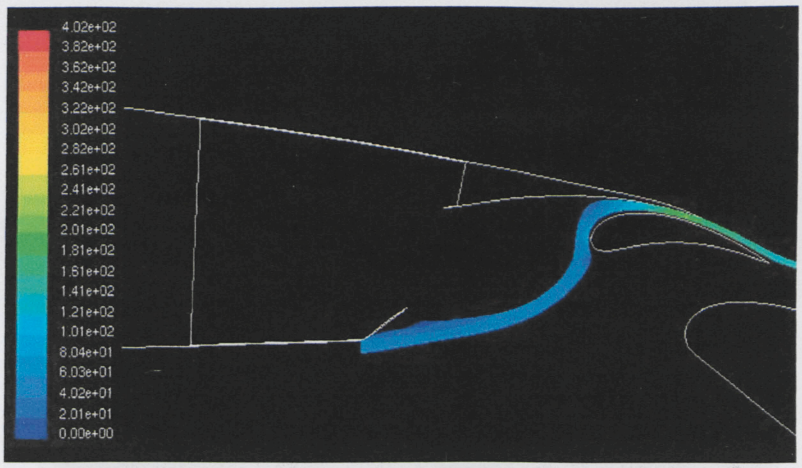

Figure 50: Pathlines Coloured by Velocity Magnitude [m/s], ½ Bute Case, α=0

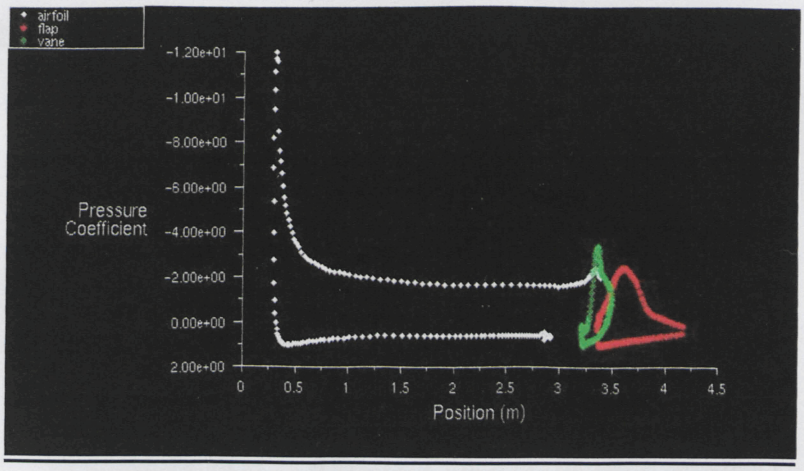

Figure 51: Pressure Distribution over the Lifting Surfaces, ½ Bute Case, α=0

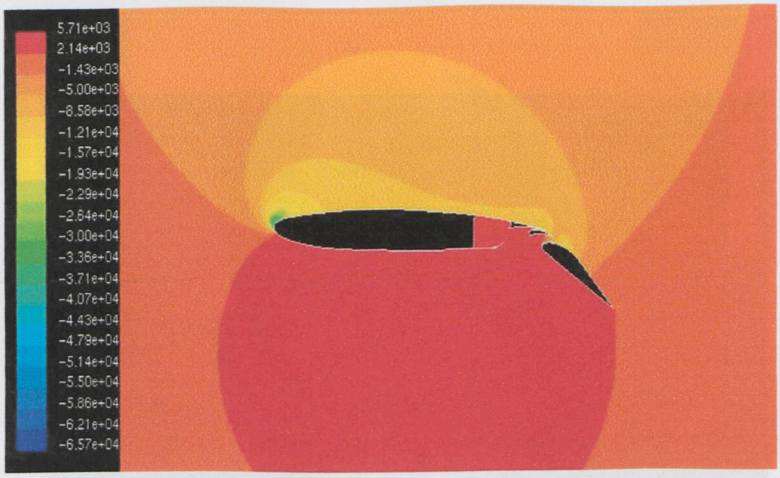

Figure 52: Contours of Static Pressure [Pa], ½ Bute Case, α=0

A.2.3 α=5

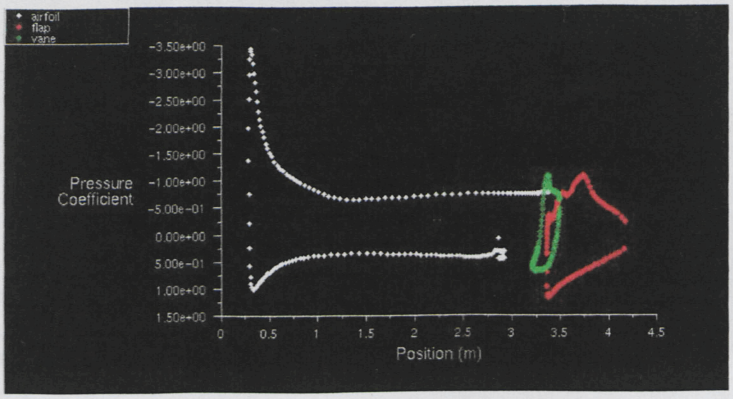

Figure 53: Pressure Distribution over the Lifting Surfaces, ½ Bute Case, α=5

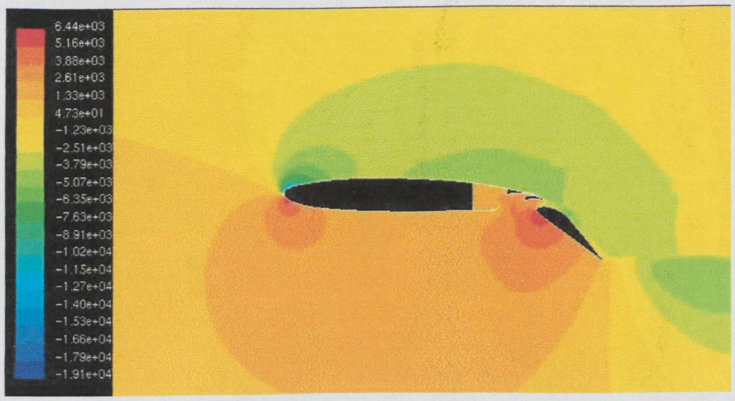

Figure 54: Contours of Static Pressure [Pa], ½ Bute Case, α=5

A.2.4 α=10

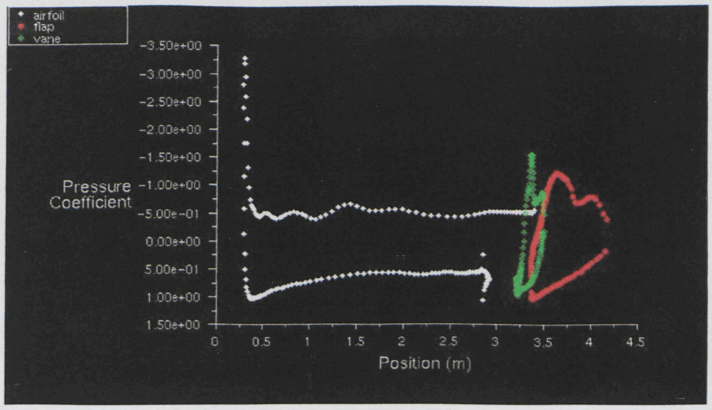

Figure 55: Pressure Distribution over the Lifting Surfaces, ½ Bute Case, α=10

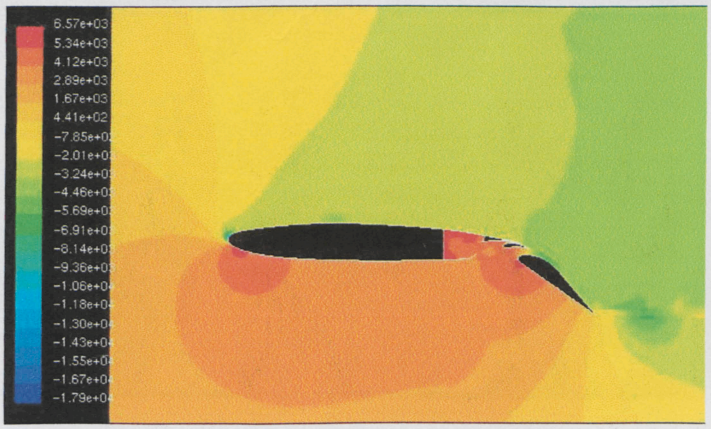

Figure 56: Contours of Static Pressure [Pa], ½ Bute Case, α=10

A.3 ¾ Bute Case Contour Plots

A.3.1 α=-5

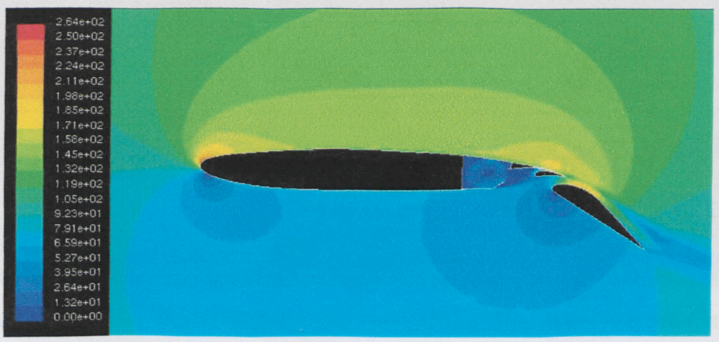

Figure 57: Contours of Velocity Magnitude [m/s], ¾ Bute Case, α=-5

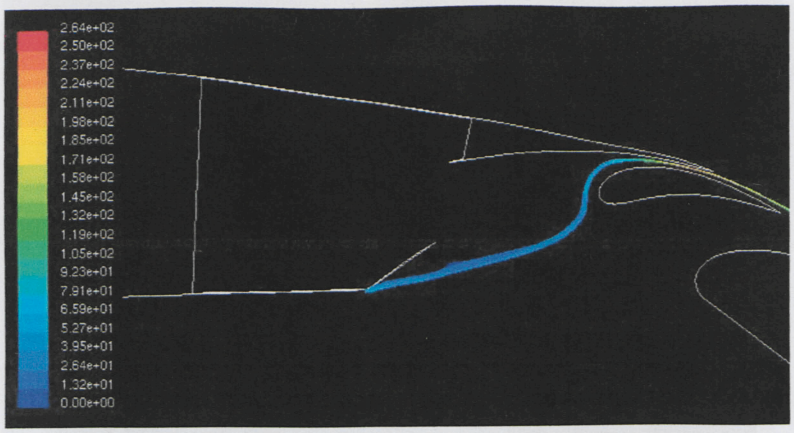

Figure 58: Pathlines Coloured by Velocity Magnitude [m/s], ¾ Bute Case, α=-5

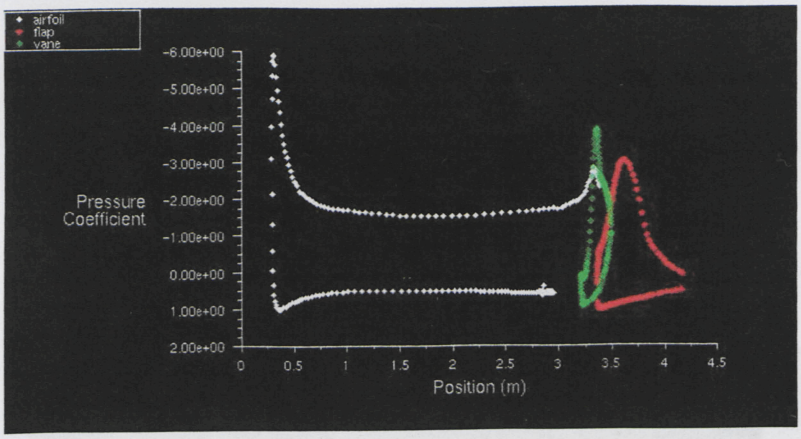

Figure 59: Pressure Distribution over the Lifting Surfaces, ¾ Bute Case, α=-5

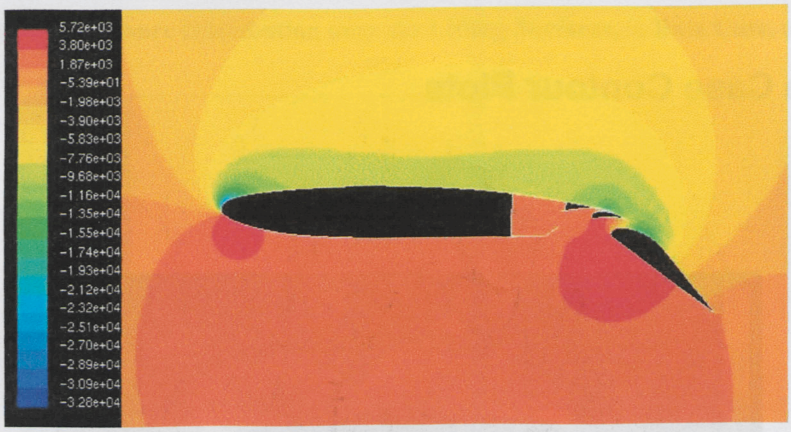

Figure 60: Contours of Static Pressure [Pa], ¾ Bute Case, α=-5

A.3.2 α=0

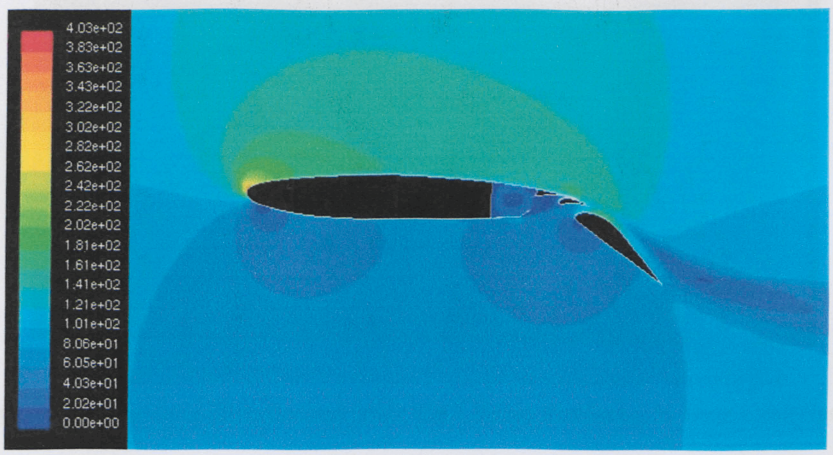

Figure 61: Contours of Velocity Magnitude [m/s], ¾ Bute Case, α=0

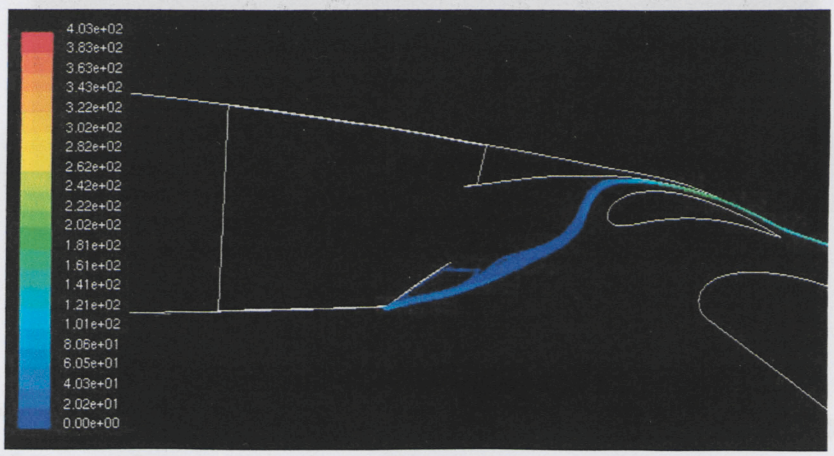

Figure 62: Pathlines Coloured by Velocity Magnitude [m/s], ¾ Bute Case, α=0

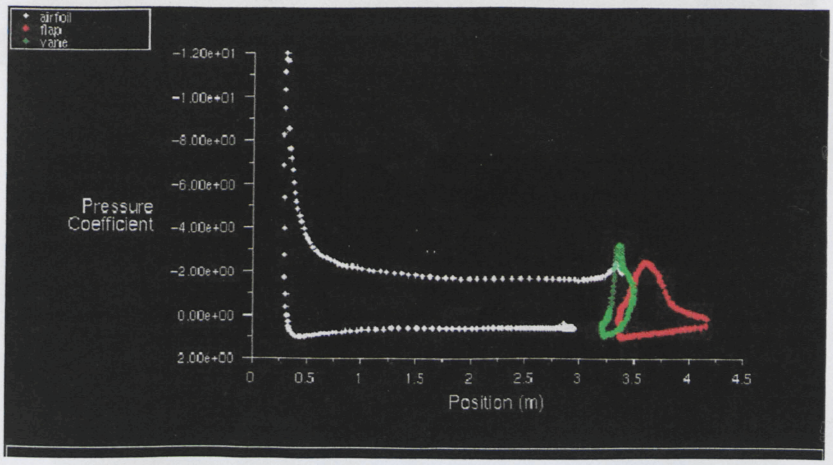

Figure 63: Pressure Distribution over the Lifting Surfaces, ¾ Bute Case, α=0

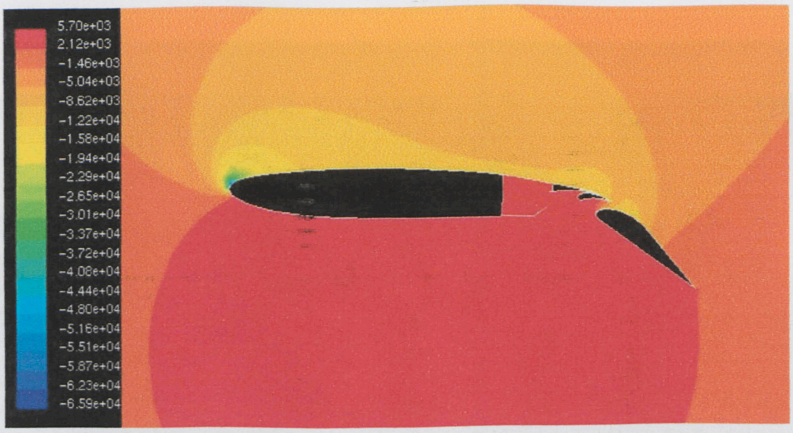

Figure 64: Contours of Static Pressure [Pa], ¾ Bute Case, α=0

A.3.3 α=5

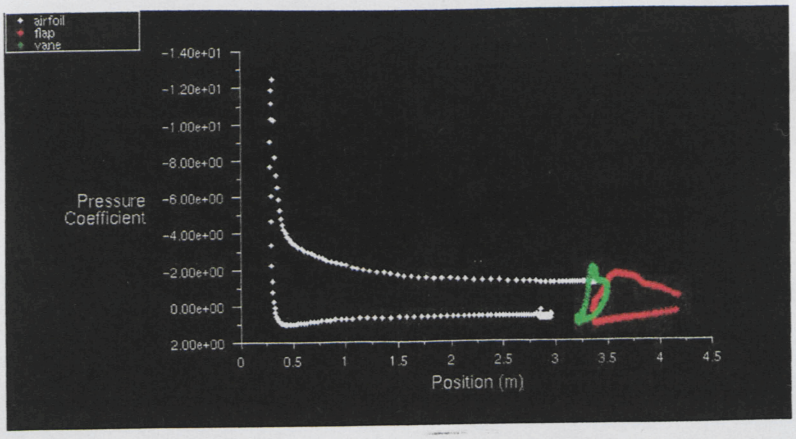

Figure 65: Pressure Distribution over the Lifting Surfaces, ¾ Bute Case, α=5

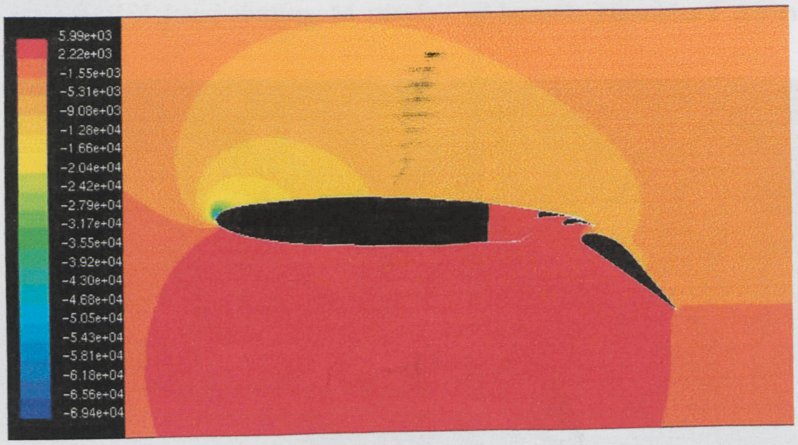

Figure 66: Contours of Static Pressure [Pa], ¾ Bute Case, α=5

A.3.4 α=10

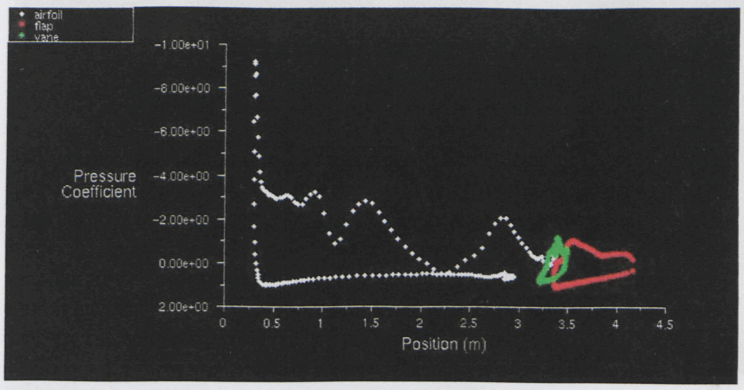

Figure 67: Pressure Distribution over the Lifting Surfaces, ¾ Bute Case, α=10

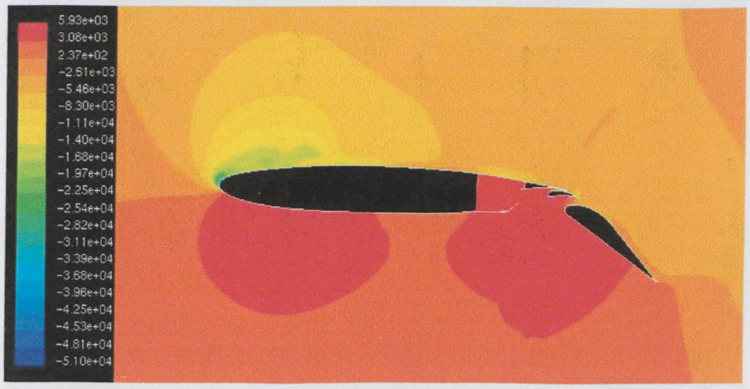

Figure 68: Contours of Static Pressure [Pa], ¾ Bute Case, α=10

A.4 25.45° Bute Case Contour Plots

A.4.1 α=-5

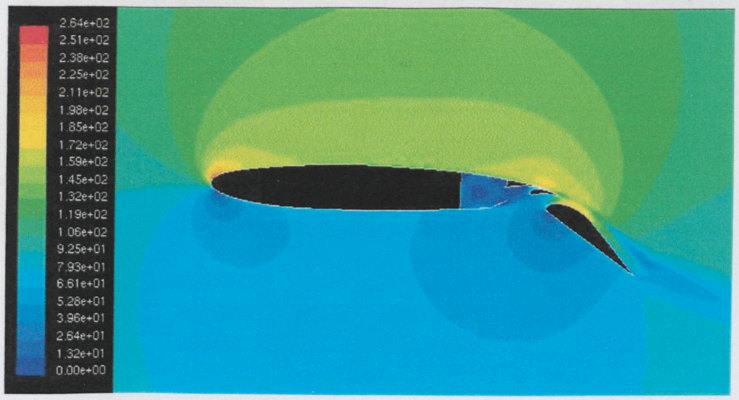

Figure 69: Contours of Velocity Magnitude [m/s], 25.45° Bute Case, α=-5

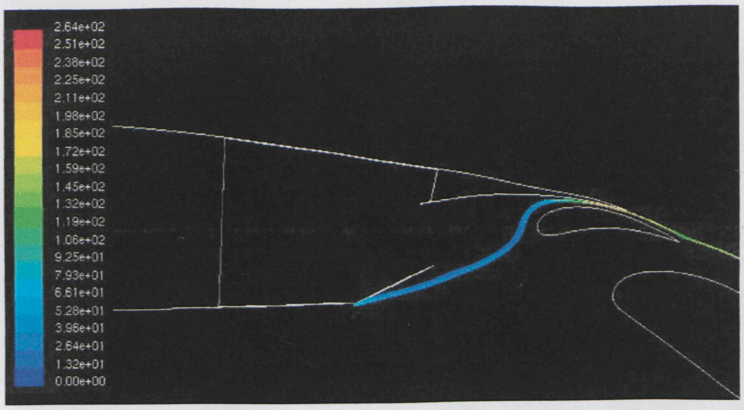

Figure 70: Pathlines Coloured by Velocity Magnitude [m/s], 25.45° Bute Case, α=-5

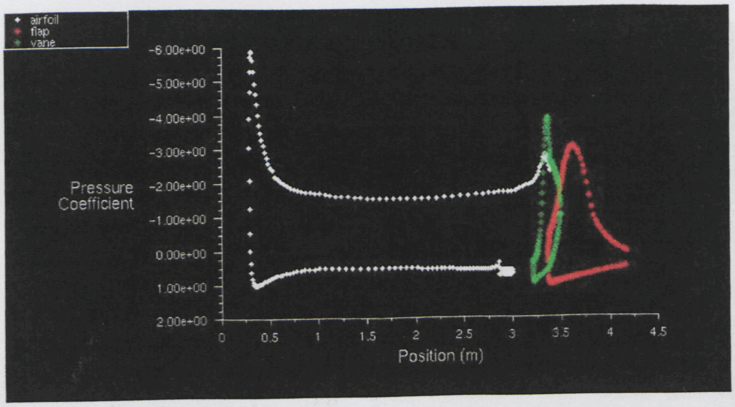

Figure 71: Pressure Distribution over the Lifting Surfaces, 25.45° Bute Case, α=-5

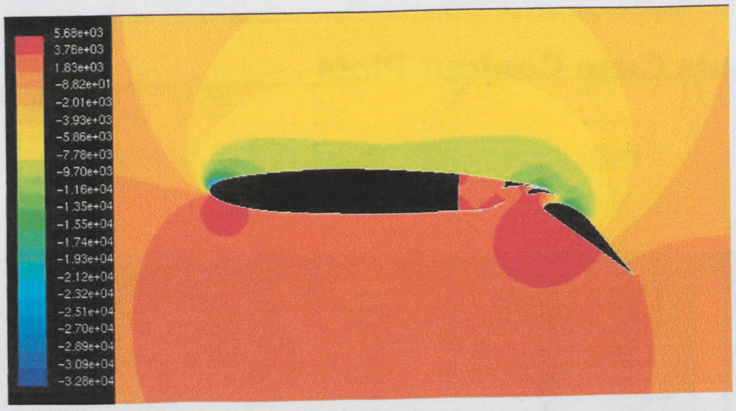

Figure 72: Contours of Static Pressure [Pa], 25.45° Bute Case, α=-5

A.4.2 α=0

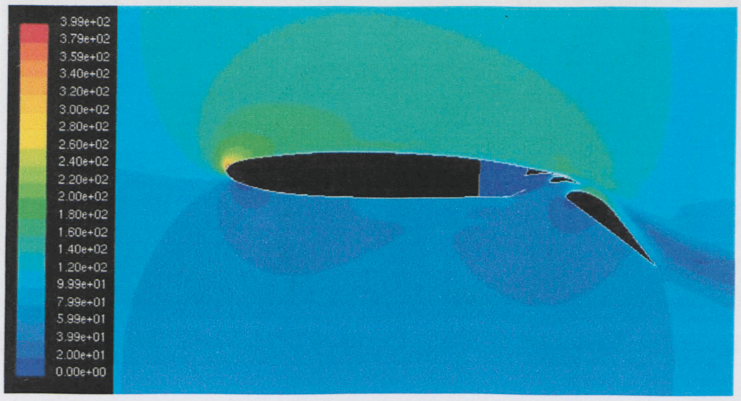

Figure 73: Contours of Velocity Magnitude [m/s], 25.45° Bute Case, α=0

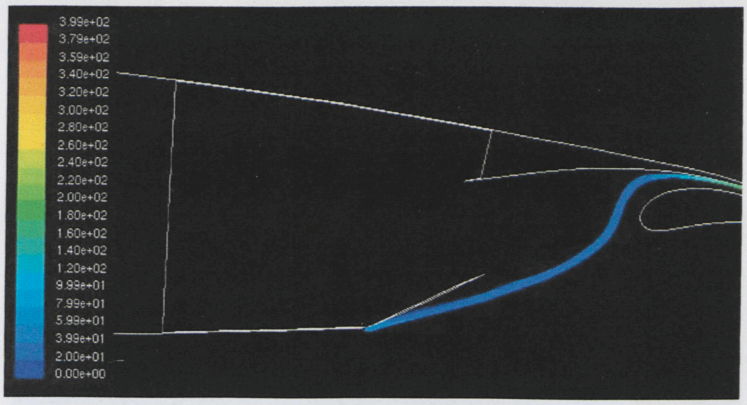

Figure 74: Pathlines Coloured by Velocity Magnitude [m/s], 25.45° Bute Case, α=0

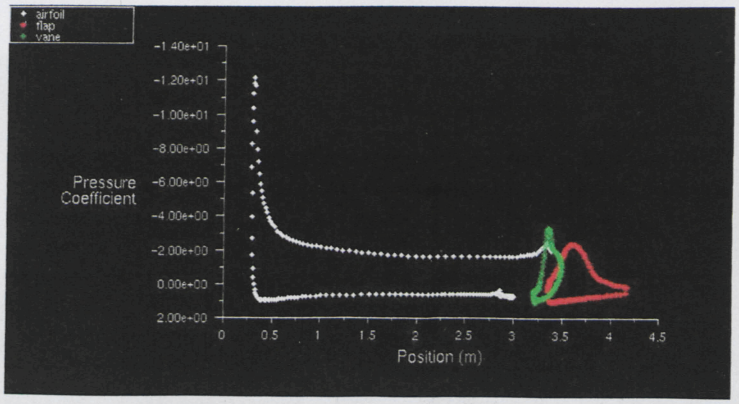

Figure 75: Pressure Distribution over the Lifting Surfaces, 25.45° Bute Case, α=0

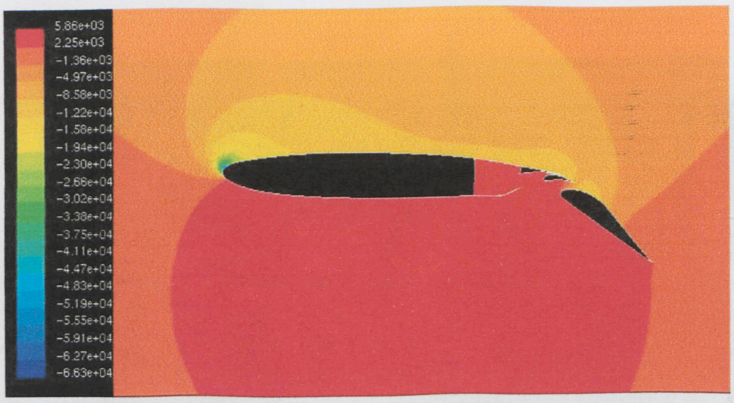

Figure 76: Contours of Static Pressure [Pa], 25.45° Bute Case, α=0

A.4.3 α=5

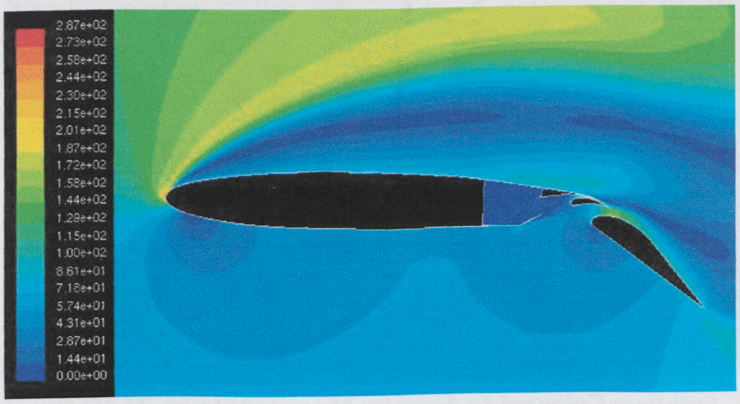

Figure 77: Contours of Velocity Magnitude [m/s], 25.45° Bute Case, α=5

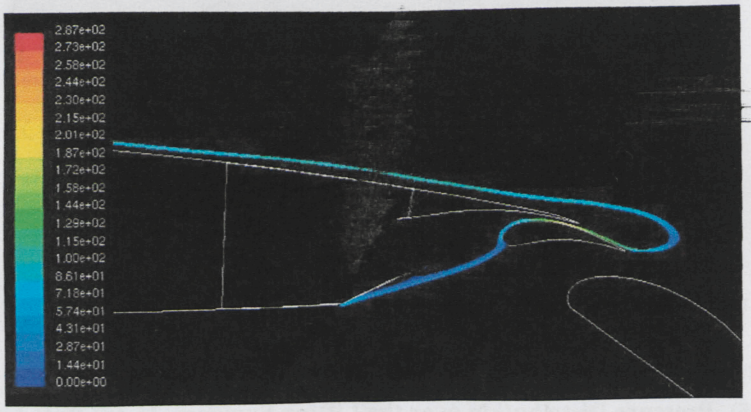

Figure 78: Pathlines Coloured by Velocity Magnitude [m/s], 25.45° Bute Case, α=5

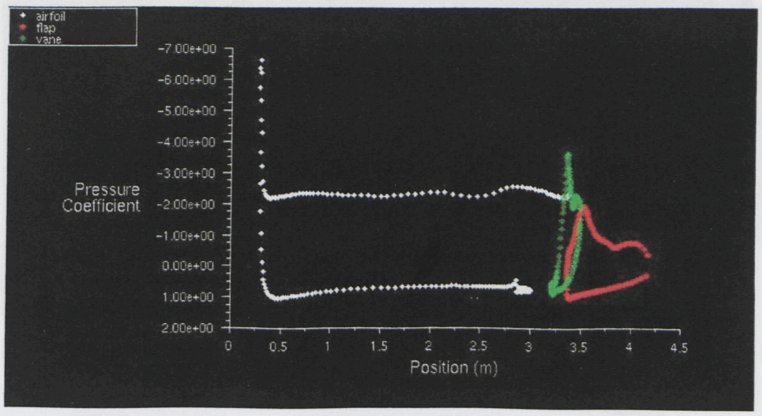

Figure 79: Pressure Distribution over the Lifting Surfaces, 25.45° Bute Case, α=5

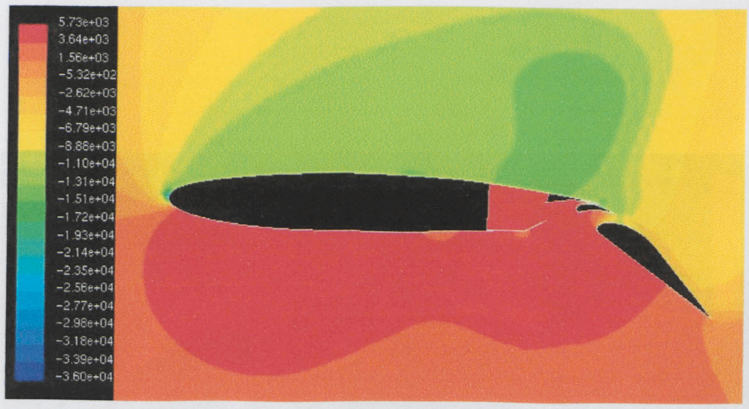

Figure 80: Contours of Static Pressure [Pa], 25.45° Bute Case, α=5

A.4.4 α=10

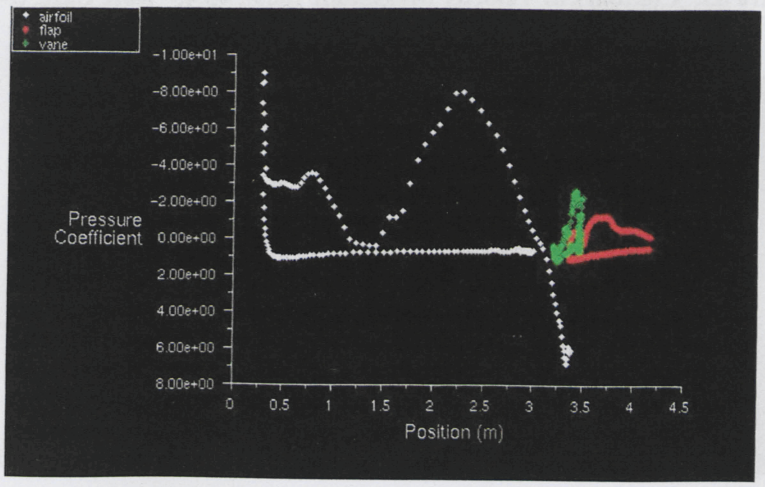

Figure 81: Pressure Distribution over the Lifting Surfaces, 25.45° Bute Case, α=10

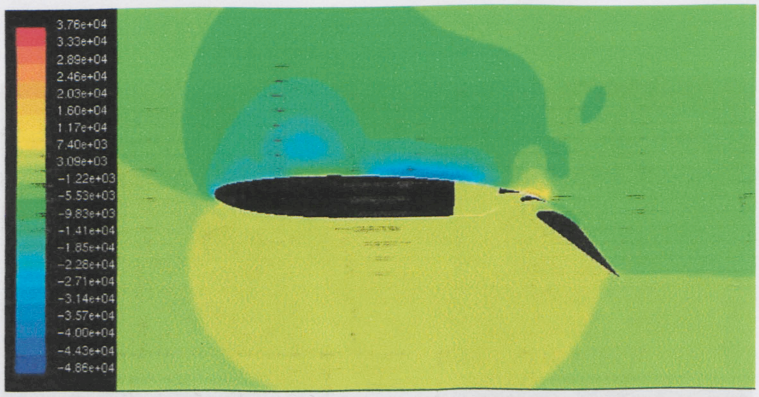

Figure 82: Contours of Static Pressure [Pa], 25.45° Bute Case, α=10

A.5 45.45° Bute Case Contour Plots

A.5.1 α=-5

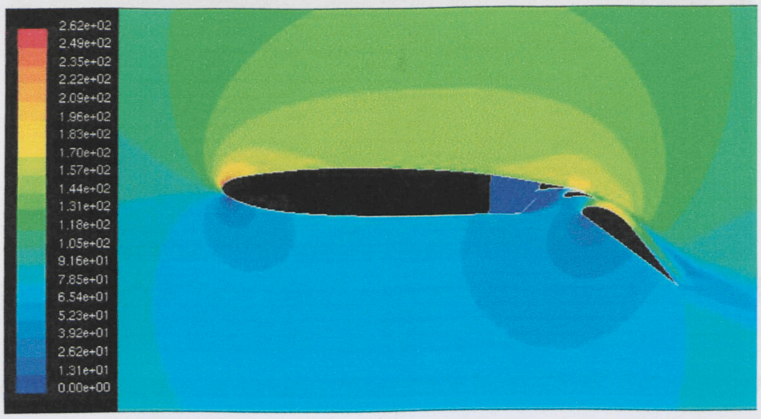

Figure 83: Contours of Velocity Magnitude [m/s], 45.45° Bute Case, α=-5

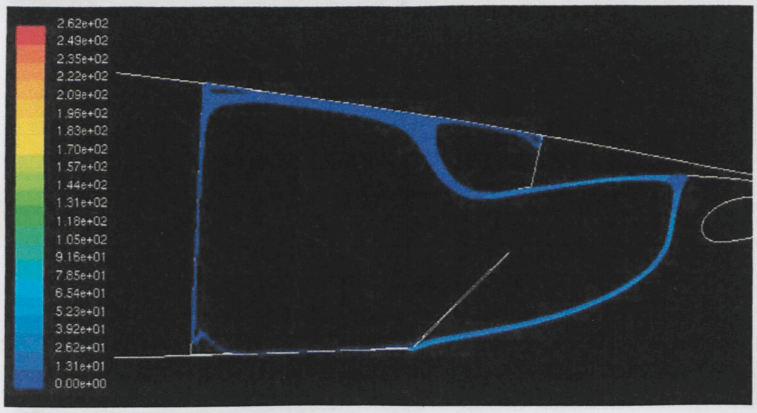

Figure 84: Pathlines Coloured by Velocity Magnitude [m/s], 45.45° Bute Case, α=-5

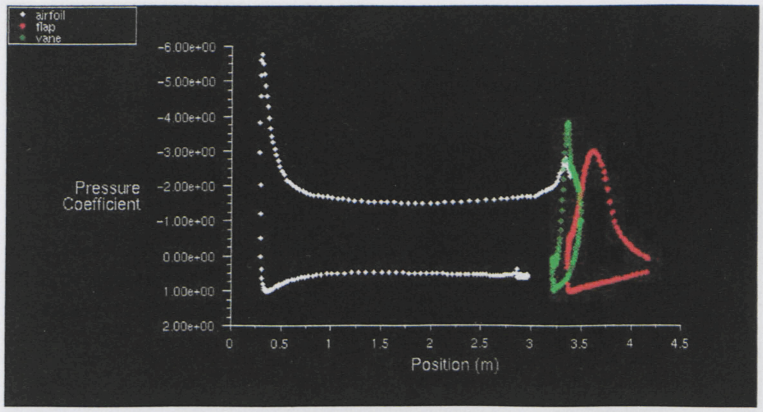

Figure 85: Pressure Distribution over the Lifting Surfaces, 45.45° Bute Case, α=-5

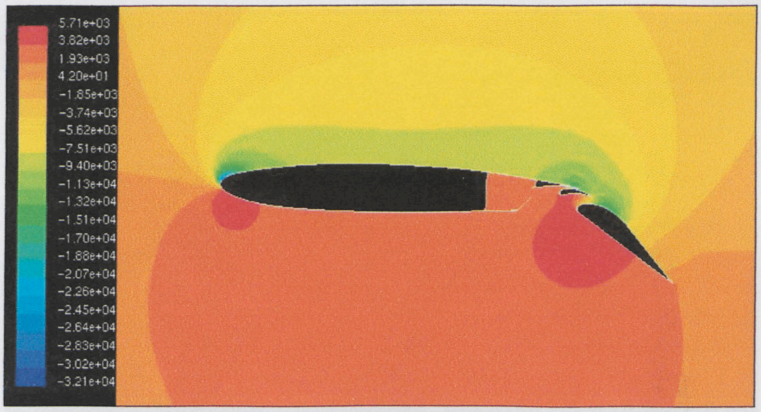

Figure 86: Contours of Static Pressure [Pa], 45.45° Bute Case, α=-5

A.5.2 α=0

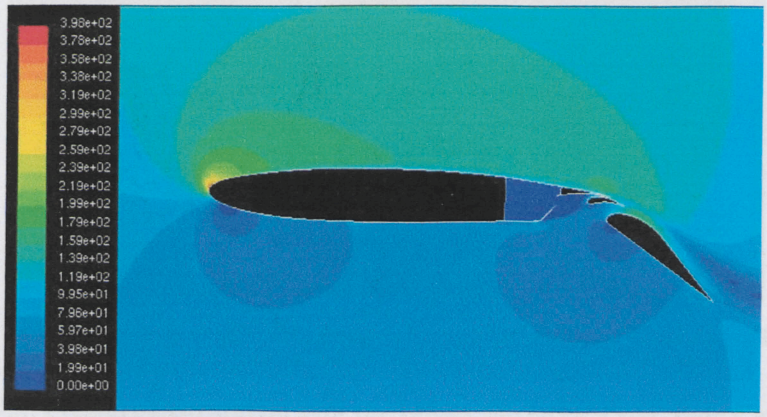

Figure 87: Contours of Velocity Magnitude [m/s], 45.45° Bute Case, α=0

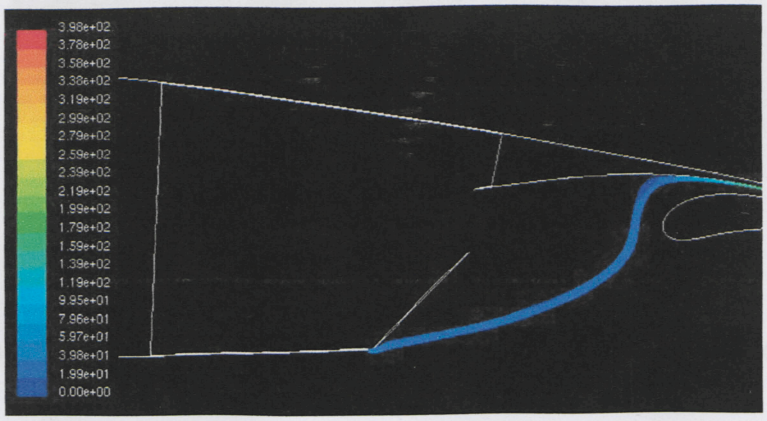

Figure 88: Pathlines Coloured by Velocity Magnitude [m/s], 45.45° Bute Case, α=0

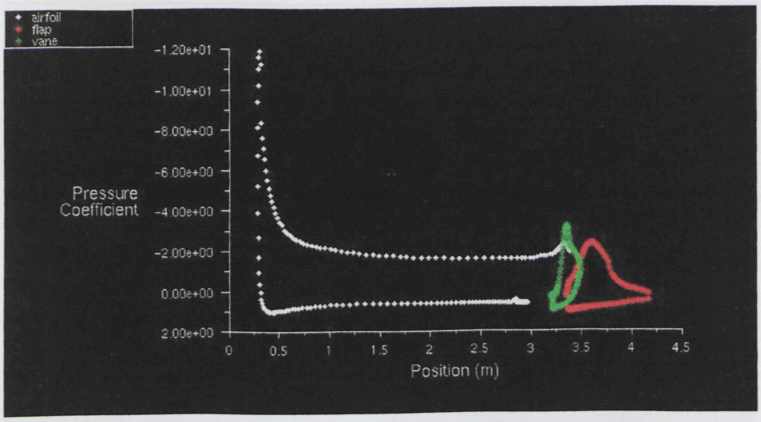

Figure 89: Pressure Distribution over the Lifting Surfaces, 45.45° Bute Case, α=0

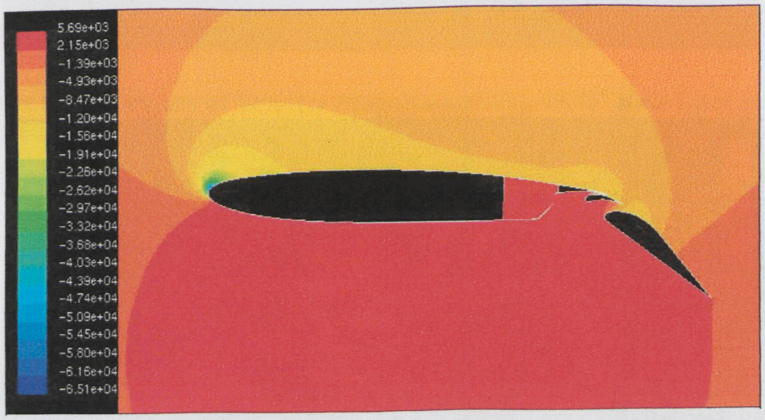

Figure 90: Contours of Static Pressure [Pa], 45.45° Bute Case, α=0

A.5.3 α=5

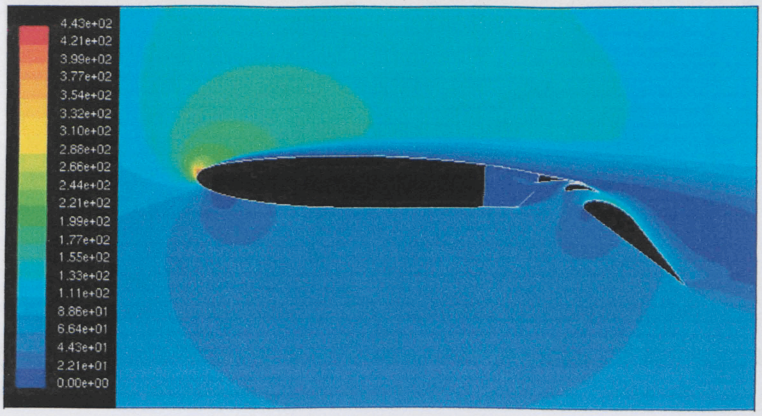

Figure 91: Contours of Velocity Magnitude [m/s], 45.45° Bute Case, α=5

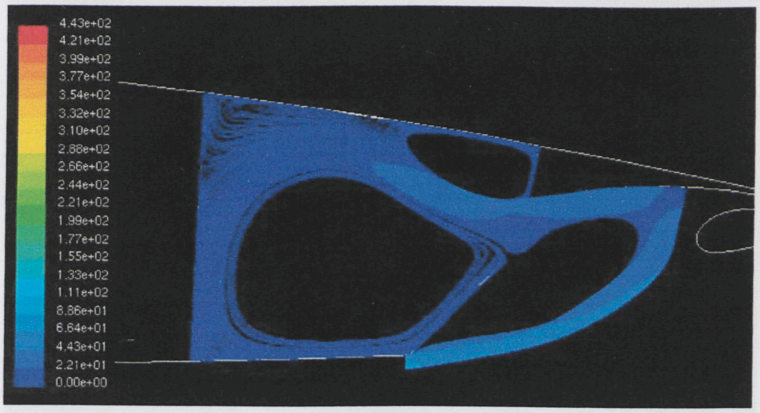

Figure 92: Pathlines Coloured by Velocity Magnitude [m/s], 45.45° Bute Case, α=5

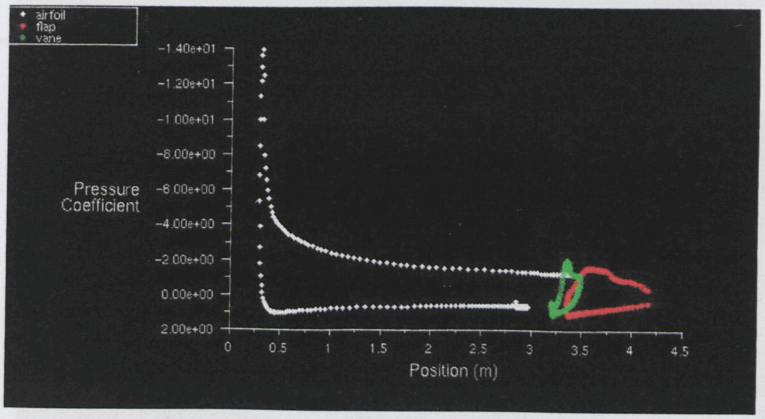

Figure 93: Pressure Distribution over the Lifting Surfaces, 45.45° Bute Case, α=5

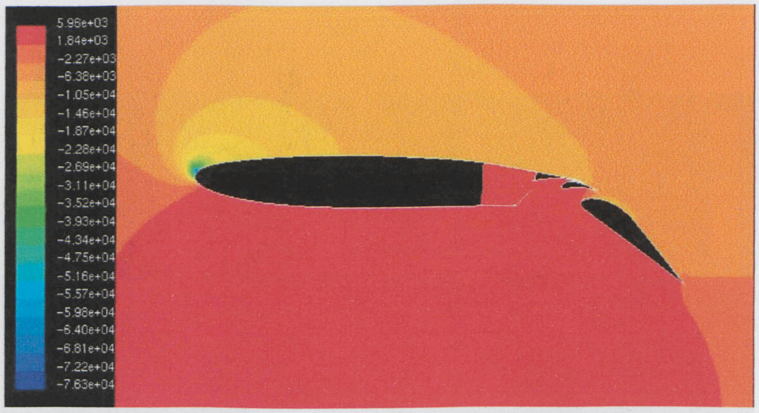

Figure 94: Contours of Static Pressure [Pa], 45.45° Bute Case, α=5

A.5.4 α=10

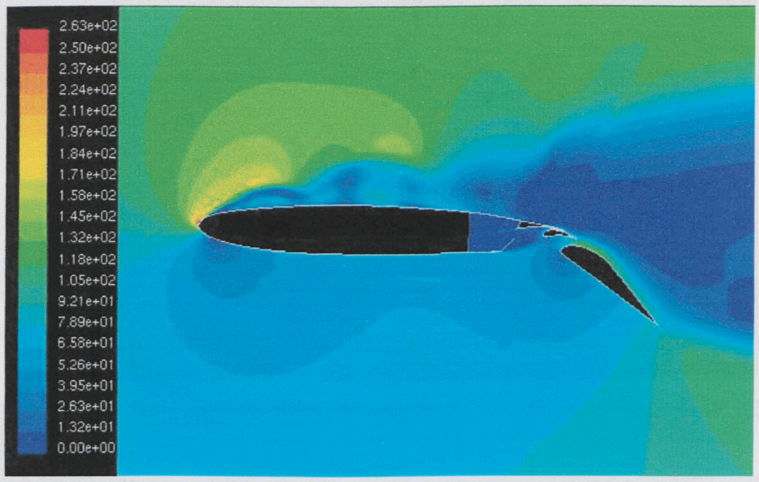

Figure 95: Contours of Velocity Magnitude [m/s], 45.45° Bute Case, α=10

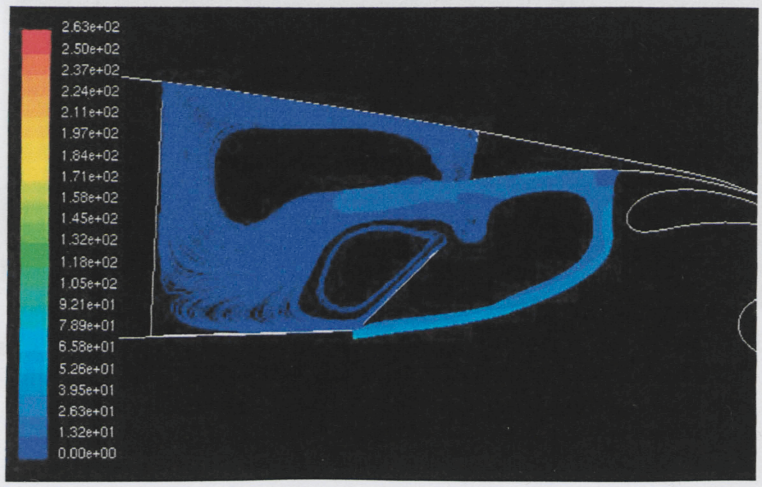

Figure 96: Pathlines Coloured by Velocity Magnitude [m/s], 45.45° Bute Case, α=10

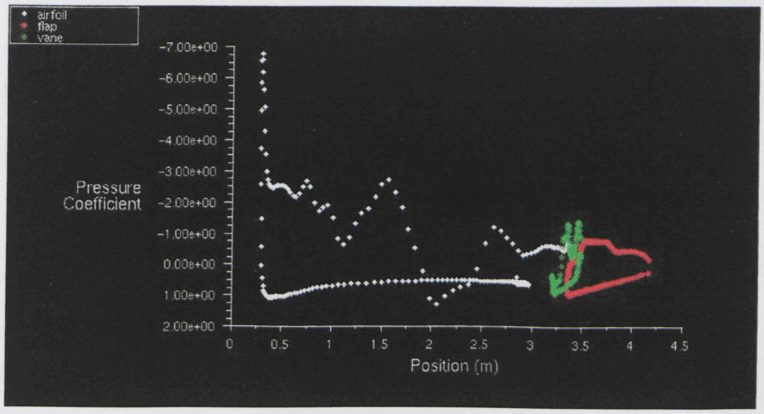

Figure 97: Pressure Distribution over the Lifting Surfaces, 45.45° Bute Case, α=10

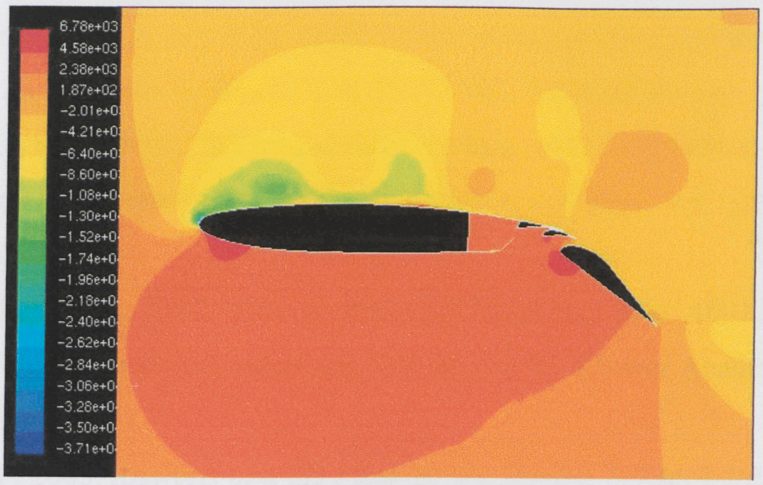

Figure 98: Contours of Static Pressure [Pa], 45.45° Bute Case, α=10

REFERENCES

1. Abbot, Ira H., Von Doenhoff, Albert E., 1959, *Theory of Wing Sections*, Dover Publications, Inc., New York.
2. Mason, W. H., *High-Lift Aerodynamics*, http://www.aoe.vt.edu/~mason/Mason_f/ConfigAeroHiLift.pdf, (September 30, 2003)
3. Lotz, Robert D., et al., 1997, "Numerical Uncertainties in Transonic Flow Calculations for Aerofoils with Blunt Trailing Edges", *International Journal for Numerical Methods in Fluids*, Vol. 24, 355-373, John Wiley & Sons, Ltd.
4. Thompson, B. E., Lotz, R. D., 2002, "Flow around a Blunt and Divergent Trailing Edge", *Experiments in Fluids*, Vol. 33, 37-383, Springer-Verlag.
5. Li, Y. C., et al., 2002, "Effects of Gurney Flaps on the Lift Enhancement of a Cropped Nonslender Delta Wing", *Experiments in Fluids*, Vol. 32, 99-105, Springer-Verlag.
6. Li, Yachen, et al., 2002, "Effects of Gurney Flaps on a NACA0012 Airfoil", *Flow, Turbulence and Combustion*, Vol. 68, 27-39, Kluwer Academic Publishers, Netherlands.
7. Hodal, P, 2003, *Analysis of a 2D Flow for the Boeing 717 high-lift devices and its response to a gradual uncovering of the spoiler*, B. Eng Thesis, Ryerson University, Toronto.
8. Stow, P., ed, 1990, *Computational Methods in Aeronautical Fluid Dynamics*, Oxford University Press, New York.
9. Reiderer, S, *Navier-Stokes Calculations of Multielement Airfoil Flows*, University of Munich, Germany.
10. FLUENT Help and Tutorial Guide.
11. Schetz, Joseph A, 1993, *Boundary Layer Analysis*, Prentice-Hall Inc., New Jersey.
12. Cebeci, Tuncer, et al., 1996, "Calculation of Multielement Airfoil Flows, Including Flap Wells", AIAA 96-0056, American Institute of Aeronautical and Astronautics Inc.

13. Aupoix, B., Spalart, P.R., 2003, "Extensions of the Spalart-Allmaras Turbulence Model to account for Wall Roughness", *International Journal of Heat and Fluid Flow,* Vol. 24, 454-462, Elsevier Science Inc.
14. Spalart, P.R., 2000, "Strategies for Turbulence Modelling and Simulations", *International Journal of Heat and Fluid Flow*, Vol. 21, 252-263, Elsevier Science Inc.